minerals

MDPI

*Article*

# Co–Mn Mineralisations in the Ni Laterite Deposits of Loma Caribe (Dominican Republic) and Loma de Hierro (Venezuela)

**Cristina Domènech [1,*], Cristina Villanova-de-Benavent [2,*], Joaquín A. Proenza [2], Esperança Tauler [2], Laura Lara [2], Salvador Galí [2], Josep M. Soler [3], Marc Campeny [4] and Jordi Ibañez-Insa [5]**

1 Grup MAiMA, Mineralogia Aplicada, Geoquímica i Geomicrobiologia, Departament de Mineralogia, Petrologia i Geologia Aplicada, Facultat de Ciències de la Terra, Universitat de Barcelona (UB), Martí i Franquès s/n, 08028 Barcelona, Spain
2 Departament de Mineralogia, Petrologia i Geologia Aplicada, Facultat de Ciències de la Terra, Universitat de Barcelona (UB), Martí i Franquès s/n, 08028 Barcelona, Spain; japroenza@ub.edu (J.A.P.); esperancatauler@ub.edu (E.T.); laauraalara17@gmail.com (L.L.); ga-li@ub.edu (S.G.)
3 Institute of Environmental Assessment and Water Research, IDAEA-CSIC, 08034 Barcelona, Spain; josep.soler@idaea.csic.es
4 Departament de Mineralogia, Museu de Ciències Naturals de Barcelona, Passeig Picasso s/n, 08003 Barcelona, Spain; mcampenyc@bcn.cat
5 Geosciences Barcelona (GEO3BCN-CSIC), Lluís Solé i Sabarís s/n, 08028 Barcelona, Spain; jibanez@geo3bcn.csic.es
* Correspondence: cristina.domenech@ub.edu (C.D.); cvillanovadb@ub.edu (C.V.-d.-B.)

**Abstract:** Cobalt demand is increasing due to its key role in the transition to clean energies. Although the main Co ores are the sediment-hosted stratiform copper deposits of the Democratic Republic of the Congo, Co is also a by-product of Ni–Co laterite deposits, where Co extraction efficiency depends, among other factors, on the correct identification of Co-bearing minerals. In this paper, we reported a detailed study of the Co mineralisation in the Ni–Co laterite profiles of Loma Caribe (Dominican Republic) and Loma de Hierro (Venezuela). Cobalt is mainly associated with Mn-oxyhydroxide minerals, with a composition between Ni asbolane and lithiophorite, although a Co association with phyllosilicates has also been recorded in a Loma de Hierro deposit. In Loma Caribe, Co-bearing Mn-oxyhydroxide minerals mainly developed colloform aggregates, and globular to spherulitic grains, while in Loma de Hierro, they displayed banded colloform, fibrous or tabular textures. Most of the compositional analyses of Mn-oxyhydroxides yielded 20 and 40 wt.% Mn, with Ni and Co up to 16 and 10 wt.%, respectively. In both profiles, Mn-bearing minerals were mainly found in the transition from the oxide horizon to the saprolite, as observed in other laterite profiles in the world, where the precipitation of Mn-bearing minerals is enhanced because of the pore solution saturation and pH increase.

**Keywords:** nickel; cobalt; manganese; lithiophorite; asbolane; critical metals; laterite



**Citation:** Domènech, C.; Villanova-de-Benavent, C.; Proenza, J.A.; Tauler, E.; Lara, L.; Galí, S.; Soler, J.M.; Campeny, M.; Ibañez-Insa, J. Co–Mn Mineralisations in the Ni Laterite Deposits of Loma Caribe (Dominican Republic) and Loma de Hierro (Venezuela). *Minerals* **2022**, *12*, 927. https://doi.org/10.3390/min12080927

Academic Editor: Maria Boni

Received: 29 June 2022
Accepted: 20 July 2022
Published: 22 July 2022



## 1. Introduction

In 2020, the European Commission published a new list of critical raw materials considered essential for the economy of Europe, according to their potential supply risk and their economic and industrial importance [1]. This list contains 30 raw materials, compared with the 14, 20 and 27 that were indicated in the previous lists of 2011, 2014 and 2017, respectively. One of these critical materials is Co, which is a transition metal that has been in the list since 2011. The main reason to consider Co as a critical raw material is that worldwide production comes primarily from the sediment-hosted stratiform copper deposits of the Democratic Republic of the Congo (accounting for 70% of the world's production) [1–3], which is also the main supplier to Europe. Cobalt is essential in many industries such aerospace, textile, electronics, automotive, renewable energies, and energy-intensive industries, where it is mainly used in batteries, super alloys, catalysts

and magnets [2]. Cobalt, together with Ni, rare earth elements (REE) and Li, is of strategic importance in the transition to cleaner energies [4,5]. Recent forecasts indicate that Europe would need up to five times more Co in 2030, and 15 times more Co in 2050 for electric vehicle batteries and energy storage, compared with the 2019 supply, this increase also being linked to the increase in demand of other metals such as Ni or Mn [1]. The strategy of EU is based on the diversification of global supply chains and the enhancement of circularity and resource efficiency.

In addition to the Congo deposits, Co is also a by-product of the mining of magmatic Ni–Cu sulphide deposits hosted in mafic and ultramafic rocks, such as Sudbury (Canada) or Norilsk (Russia), and of Ni–Co laterite deposits in Australia, New Caledonia, Indonesia, the Philippines, Brazil, Cameroon, Greece and the Caribbean region ([2,3,6] and references therein). Cobalt content in laterite deposits is estimated to comprise 36% of terrestrial Co deposits [7]. Cobalt has also been identified in manganese nodules and crusts on ocean floors [3].

Ni–Co laterite deposits result from the weathering of ultramafic rocks (generally serpentinised peridotites) at tropical latitudes [8–11]. In a typical Ni–Co laterite profile, the unaltered or serpentinised peridotite is found at the bottom, covered by a saprolite horizon that contains relicts of the parent rock with secondary serpentine, goethite and Mg–Ni phyllosilicates. An oxide horizon is formed over the saprolite zone, consisting of Fe-(goethite, hematite, maghemite), Al-(gibbsite) and occasionally, Mn-oxides and hydroxides. In some cases, an iron cap or ferricrete has developed over the oxide horizon. According to the main Ni mineralogy, Ni–Co laterites are classified into oxide type (where Ni is mainly associated with Fe-oxyhydroxides), clay silicate type (where Ni is concentrated in smectite group minerals), and hydrous silicate type (rich in Mg–Ni phyllosilicates, including Ni-serpentines and garnierites) ([8,12] and references therein). Cobalt is usually accumulated within the ferruginous unit or at the transition from the saprolite to the oxide horizon, and is mostly concentrated into poorly crystalline Fe- and Mn-oxyhydroxides.

Although in some deposits Co is found in primary minerals (e.g., sulphides, carbonates), in their alteration products (e.g., heterogenite (CoOOH)), or in laterite deposits, Co is usually associated with Mn-oxyhydroxides, in particular, asbolane, lithiophorite, or the so-called asbolane–lithiophorite intermediates [13].

Due to the low grade, its irregular distribution, and the complex mineralogy of the ores, the Co-production from laterite ores is generally low [14,15]. Moreover, the Co beneficiation mainly depends on its oxidation state and the relative proportion of Co to Cu or Ni [13]. Therefore, a proper identification and characterisation of Co-bearing minerals in the context of a laterite deposit is relevant, in order to improve the extraction efficiency. Recently, the number of studies dealing with how Co (and also Ni, Mn and Sc) are distributed in these deposits, have increased [6].

There are large Ni–Co laterite deposits with economic grades of Co (e.g., Murrin Murrin or Kalgoorlie in Australia, Goro in New Caledonia, or Nkamouna in Cameroon) [2]. However, recent studies have pointed out that Ni–Co laterites from the Caribbean area also contain significant amounts of Co that could be exploited in the near future [16–18].

Therefore, in this study we present a detailed characterisation of Mn-bearing minerals of two profiles from two Caribbean Ni–Co laterite deposits, with the goal of determining their mineralogy and composition and ultimately understanding their formation processes. More precisely, the study is centered in the Loma Caribe and the Loma de Hierro profiles, for which no previous work on manganese mineralisations is available. This study also aims to compare the Co-Mn-bearing phases identified in the Caribbean area with those reported in other deposits worldwide.

## 2. Geological Setting

The Loma Caribe Ni laterite deposit belongs to the Falcondo mining area, located in the central part of the Dominican Republic, in the northern Caribbean (Figure 1a). This deposit, together with other six other satellite deposits ([16] and references therein) developed

during the Miocene after weathering of the Loma Caribe peridotite, which occurs as a serpentinised belt of ultramafic rocks, approximately 4–5 km wide and 95 km long, NW of Santo Domingo (Figure 1b). The Loma Caribe peridotite represents a harzburgitic oceanic mantle, as part of a dismembered Cretaceous ophiolitic complex [19]. The Loma Caribe deposit is classified as hydrous Mg silicate type, and, based on its geochemical footprint, textures and mineralogy, has been divided into several zones, which are, from bottom to top, the serpentinised peridotite, the saprolite horizon, the oxide horizon and a duricrust zone [16]. The protolith is a serpentinised peridotite rich in olivine and enstatite, crosscut by serpentine minerals (i.e., lizardite). The saprolite horizon consists of Ni-rich lizardite with relicts of olivine and enstatite, and with minor clinochlore, maghemite and goethite. In the oxide horizon, ore samples contain goethite, hematite, gibbsite and chromian spinel [16] (Figure 2).

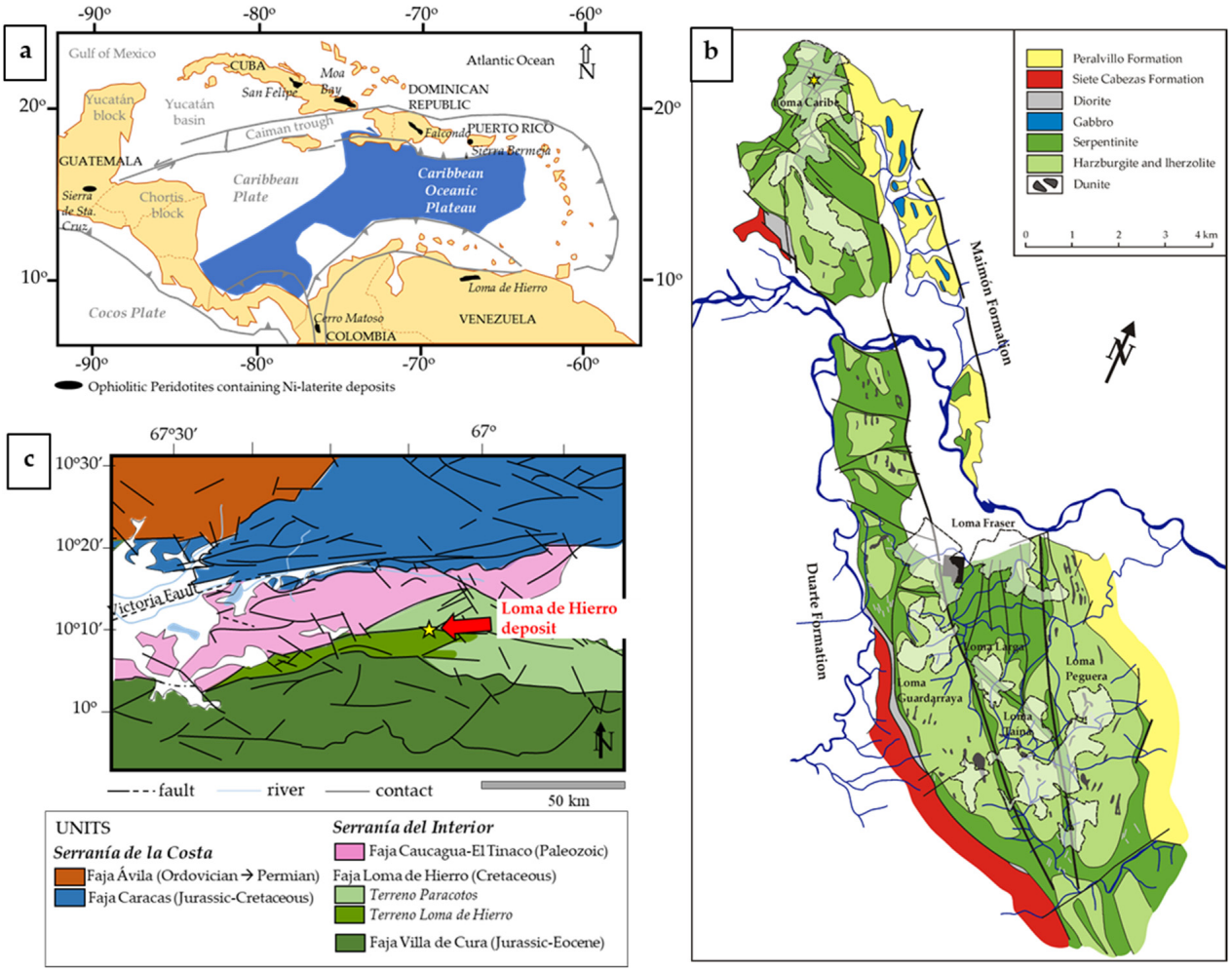


**Figure 1.** Loma Caribe (Dominican Republic) and Loma de Hierro (Venezuela) Ni laterite deposits: (**a**) location in the Caribbean region; (**b**) geological map of Loma Caribe (redrawn from [18]); and (**c**) geological map of Loma de Hierro (simplified from [20]).

Ore minerals are mainly secondary Ni serpentine and garnierites (fine grained, poorly crystalline, Ni-bearing serpentine, talc, chlorite, smectite and sepiolite) [16,18]. The Falcondo mining district has 67.8 Mt of indicated Ni resources at an average grade of 1.5 wt.% Ni [16].

The Loma de Hierro laterite deposit is located in the northcentral part of Venezuela. This deposit is placed on the Faja Loma de Hierro, which belongs to an elongated, deformed belt in the Caribbean Plate southern margin (Figure 1a), represented by the Cretaceous Dutch and Venezuelan Islands and the Cordilleras of Venezuela [21] (Figure 1c).

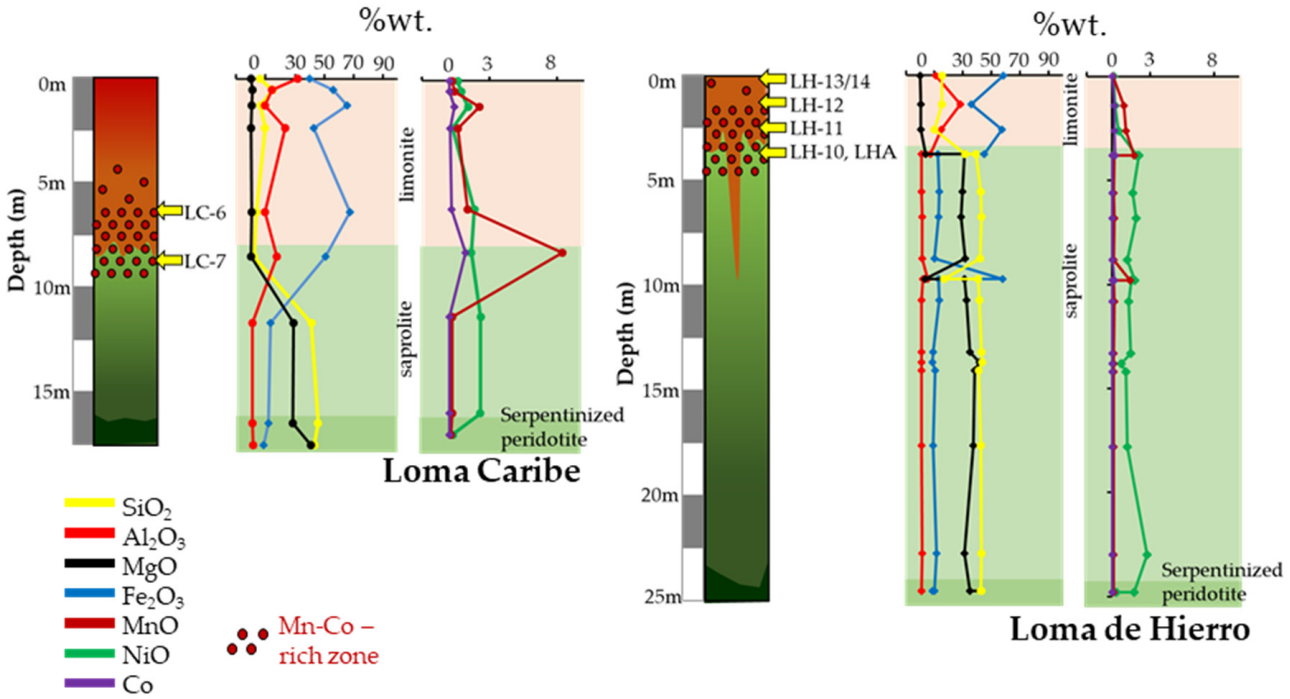


**Figure 2.** Ni–Co laterite profile from Loma Caribe (Falcondo, Dominican Republic) and Loma de Hierro (Venezuela) ore deposits, showing the location of the samples studied in this paper with major and relevant minor element contents.

The exploited area has a length of ~15 km and a width of 1 to 7 km [17]. This deposit formed over the partially serpentinised peridotites of the Loma de Hierro ophiolite, a W–E aligned unit (~100 km$^2$) within the Serranía de la Costa in the south Caribbean Plate margin (Figure 1) [21,22]. The Loma de Hierro ophiolite is made up of harzburgite and dunite (Loma de Níquel mantle peridotite), gabbros (Gabro de Mesia; 127 + 1.9/−4.3 Ma) and basaltic rocks with MORB affinity (Basalto de Tiara) [23–25]. Several studies [24,25] have described the Loma de Hierro ophiolite as being a fragment of proto-Caribbean lithosphere.

The Loma de Hierro deposit is also considered as a hydrous Mg silicate type Ni deposit, developed from a partially serpentinised harzburgite peridotite. Over this peridotite, and as in the case of Loma Caribe, several horizons have been defined: lower saprolite, upper saprolite and a poorly developed oxide zone [17]. The protolith is comprised of olivine and orthopyroxene, with minor amounts of lizardite, chrysotile, kerolite and chlorite. The lower saprolite contains large amounts of olivine, orthopyroxene, lizardite and chrysotile. In some samples, the presence of garnierites is observed. The upper saprolite is poorer in olivine and orthopyroxene, and richer in lizardite, chrysotile, kerolite and chlorite. The saprolite zone is enriched in Ni (1.1–2.7 wt.% NiO). The oxide zone is characterised by high contents of goethite, hematite and gibbsite. Ore minerals are secondary Ni serpentine and Ni-rich kerolite–pimelite garnierite mixtures (~22 wt.% NiO).

Economic concentrations of Mn and Co are observed in both profiles. Co–Mn mineralisations mainly occur as fine-grained, black, semi-metallic or dull coatings and open space infillings near the transition between the oxide and the saprolite horizons (Figure 3).

In Loma Caribe, two Mn–Co-rich levels have been described: (i) at the transition zone between the saprolite and the oxide horizon (8.4 wt.% MnO; 1.23 wt.% Co); (ii) at the lower part of the upper oxide zone (2.2 wt.% MnO; 0.4 wt.% Co) [16]. In Loma de Hierro deposit, the MnO and Co reach grades of up to 1.40 wt.% and 0.14 wt.%, respectively [17].

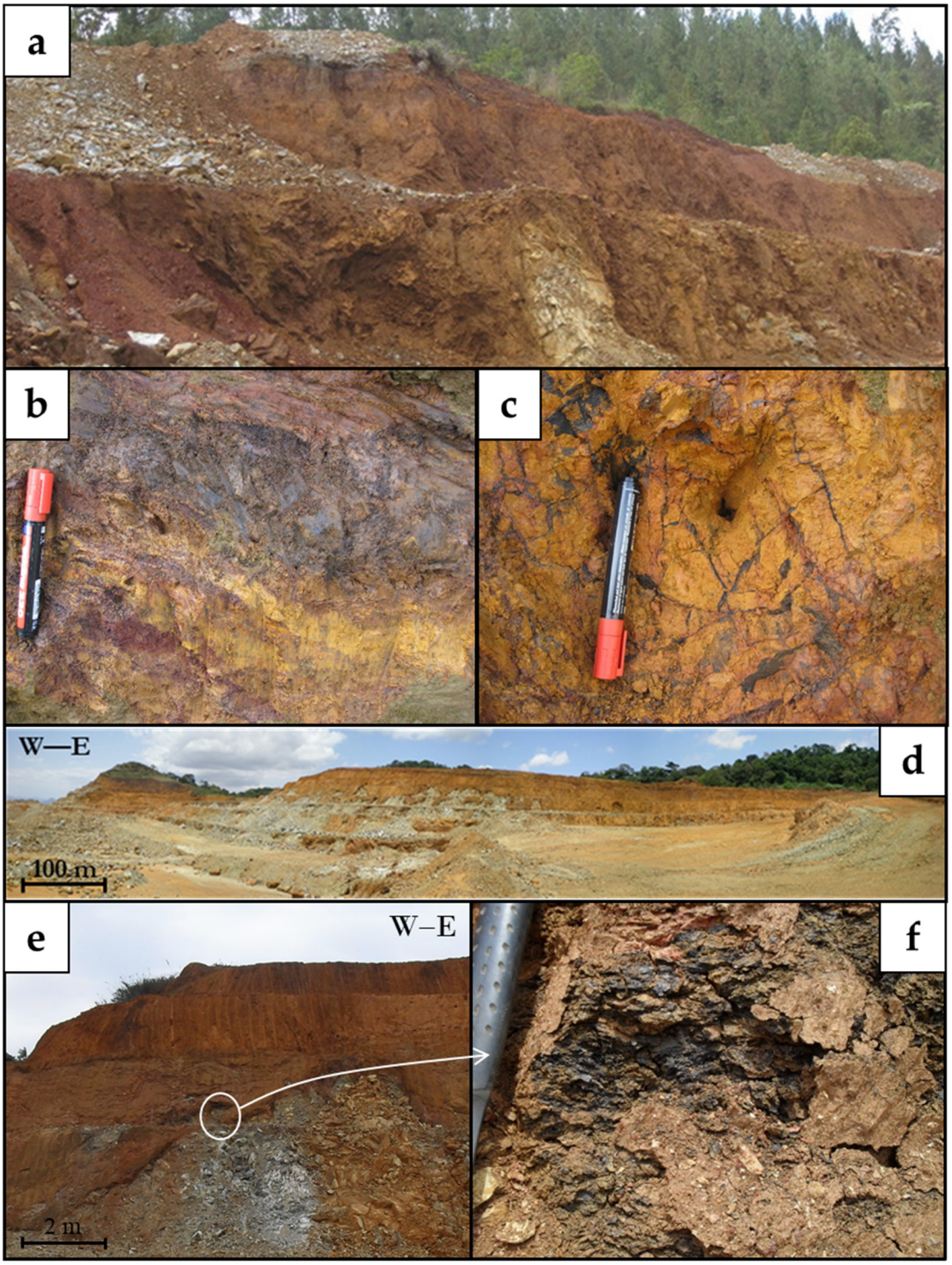


**Figure 3.** Field occurrence of Co–Mn mineralisations in Loma Caribe (**a**–**c**) and Loma de Hierro (**d**–**f**). Panorama view of the mining pits (**a**,**d**,**e**) and close-up views of Co–Mn mineralisations (**b**,**c**,**f**).

## 3. Materials and Methods

### *3.1. Sampling and Sample Preparation*

A total of seven samples were selected for the present study, two from Loma Caribe, (LC-6 and LC-7) and five from Loma de Hierro (LH-10, LH-11, LH-12, LH-13/14, and LHA) (Figure 2). All samples except LHA have been studied previously [16,17] but they have been revisited here with a focus on Mn–Co-bearing minerals. Sample LHA from Loma de Hierro was collected from a Mn–Co rich zone, and was divided into two subsamples according to their colour, which were named LHA-1 (whitish sample) and LHA-2 (blackish sample).

### *3.2. Analythical Methods*

Samples LC6, LC7, a subsample of LC7 with higher concentration of blackish material (rich in Mn-oxyhydroxides) named LC7_black, and samples LHA-1 and LHA-2 were analysed using X-ray powder diffraction (XRPD). Samples were powdered using an agate mortar and pestle. XRPD analysis was carried out at the Centres Científics i Tecnològics of the Universitat of Barcelona (CCiT-UB) with a PANalytical X'Pert PRO MPD Alpha1 powder diffractometer in Bragg–Brentano θ/2θ geometry of 240 mm of radius, nickel filtered Cu Kα1 radiation (λ = 1.5406 Å), 45 keV and 40 mA. The samples were scanned from 4 to 100° (2θ) with a step size of 0.017° and a measuring time of 150 s per step, using an X'Celerator detector (active length = 2.122°) and a variable divergence slit. Mineral identification was performed by X'Pert Highscore search–match software using the Powder Diffraction File (PDF-2) of the International Centre for Diffraction Data (ICDD), and quantitative mineral phase analyses were obtained by full profile Rietveld refinement using XRPD data and TOPAS V4.2 software [26,27]. Sample LH-10 was also analysed by powder angle-dispersive micro-XRD in the microdiffraction/high-pressure station of the BL04-MSPD beamline at ALBA Synchrotron, Barcelona. This beamline is equipped with a Kirkpatrick–Baez mirror that allows a focus of the monochromatic beam to around 15 μm × 15 μm (full width at half maximum) with a Rayonix SX165 CCD detector.

For the above measurements, a wavelength of 0.4246 Å was selected, as determined from the absorption K-edge of Sn (29.2 keV). The data were acquired by using the synchrotron through-the-substrate X-ray microdiffraction technique [28]. Small amounts of powdered material were placed on top of a Kapton® tape attached to a glass substrate. The sample-to-detector distance and the beam centre position was calibrated from $LaB_6$ diffraction scans obtained under exactly the same conditions as the sample. The calibration and subsequent integration of the CCD images were performed with Dioptas software [29]. Phase identification on the integrated powder scans was carried out by using the package Diffrac.EVA from Bruker, together with the Powder Diffraction File (PDF-2) and the Crystallography Open Database (COD).

Samples LC6, LC7, LC7_black, LHA-1 and LHA-2 were analysed by differential thermal analysis coupled with thermogravimetry (DTA-TG) using a Netzsch STA 409C/CD instrument. Approximately 150 mg of powdered sample was put in an alumina crucible under a $N_2$(g) atmosphere with a flow rate of 80 mL $min^{-1}$, in a range between 25 to 800 °C at 10 °C $min^{-1}$ using ~80 mg of an alumina standard (Perkin-Elmer 0419-0197). The same powder samples were analysed by Fourier transform infrared spectroscopy (FTIR) using a 2000 FTIR spectrometer (Perkin–Elmer System, Waltham, MA, USA) at a range for vibrational spectra of 400–4000 $cm^{-1}$, at the Departament de Mineralogia, Petrologia i Geologia Aplicada de la Facultat de Ciències de la Terra (Universitat de Barcelona).

The major, minor and trace element compositions discussed in this paper were drawn from references [16,17] except data for sample LHA that were obtained by X-ray fluorescence (XRF) and inductively coupled mass spectrometry (ICP-MS; after acid dissolution) at the Actlabs Laboratories (Ontario, Canada) as described in the aforementioned papers.

Polished sections and polished thin sections of the selected samples were examined under a transmitted and reflected light optical microscope at the Departament de Mineralogia, Petrologia i Geologia Aplicada de la Facultat de Ciències de la Terra (Universitat de Barcelona), while samples containing Co and Mn mineralisations were carbon coated and studied in a scanning electron microscope (SEM) Quanta 200 FEI, XTE 325/D8395, with an INCA energy dispersive spectrometer (EDS) microanalysis system, and a field emission SEM (FE-SEM) Jeol JSM-7100 equipped with an INCA Energy 250 EDS, under 20 kV and 5 nA, at the CCiT-UB. Co–Mn-bearing minerals were analysed by electron microprobe analyser (EMPA) at the CCiT-UB by using a JEOL JXA-8230 electron microprobe, equipped with five wavelength-dispersive spectrometers and an energy-dispersive spectrometer. The operating conditions were 20 kV accelerating voltage, 15 nA beam current, 2 μm beam diameter and a counting time of 20 s per element. The calibration standards used were: wollastonite (Si, Ca), corundum (Al), orthoclase (K), hematite (Fe), periclase (Mg), rhodonite

(Mn), NiO (Ni), metallic Co (Co), rutile (Ti), albite (Na), $Cr_2O_3$ (Cr), V (V), Sc (Sc), and baryte (Ba).

Thermodynamic calculations were carried out with GibbsStudio software [30] based on the PHREEQC code [31] and the thermodynamic data llnl.dat database supplied with PHREEQC code and modified, when specified, to complete Co and Mn aqueous species and solid-phases thermodynamic data.

## 4. Results

### *4.1. Mineralogy and Petrography*

In Loma Caribe deposits, and according to XRPD (samples LC-6, LC-7 and LC-7_black), lithiophorite is ubiquitous with clear peaks at 9.3 and 4.7 Å (Figure 4a,b). Those $d_{hkl}$ are comparable to those obtained by Burlet and Vanbrabant [32] (9.45 and 4.69 Å in lithiophorite, 4.76 Å in asbolane, and 9.59 and 4.76 Å in lithiophorite–asbolane intermediates), and by Putzolu and co-authors [15] (4.84 Å in asbolane), confirming the observations by Aiglsperger and co-authors [16]. Gibbsite, goethite and chromite were also identified in those samples. High concentrations (12%) of lithiophorite were quantified by Rietveld in sample LC-7_black (Figure 4b).

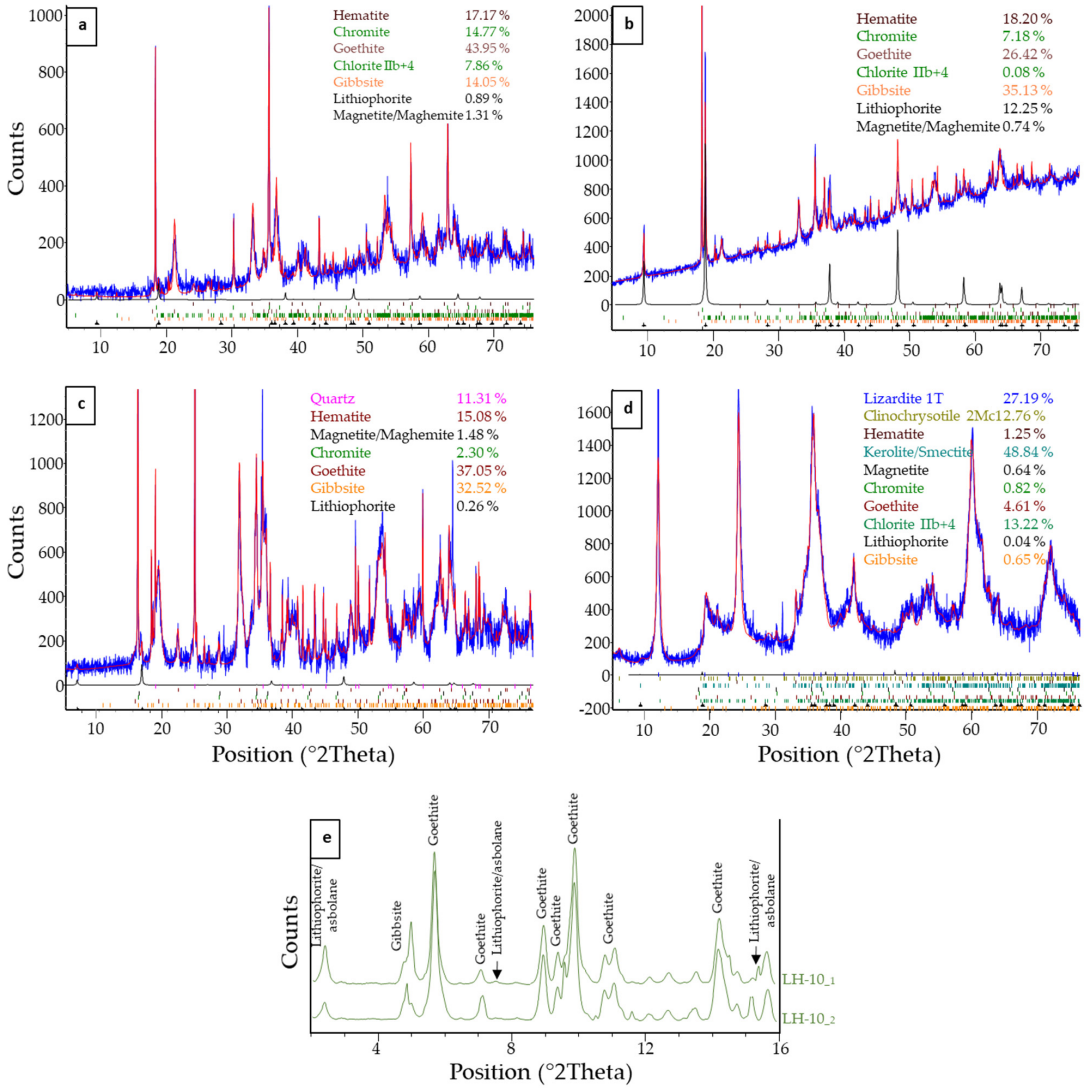


**Figure 4.** (**a**–**d**) X-ray diffraction patterns obtained for samples LC-6 (**a**), LC-7-black (**b**), LH-11 (**c**), and LH-10 (**d**). In blue, experimental data; in red, Rietveld fit, and in black, lithiophorite spectra. Mineral percentages obtained after Rietveld interpretation (λ = 1.5406 Å). (**e**) Two micro-XRD measurements of sample LH-10 obtained at ALBA synchrotron (λ = 0.4246 Å).

Although in minor amounts (up to 0.3%), lithiophorite was also identified in the Loma de Hierro samples (Figure 4d,e). The main mineral phases were goethite, gibbsite, quartz, lizardite and smectite. Micro-XRD scans of sample LH-10 (Figure 4e) were dominated by typical XRD peaks of goethite. However, whereas the LH-10_$_2$ curve exhibited the XRD signature of gibbsite, the LH-10_$_1$ curve showed several features that can be attributed to lithiophorite and/or asbolane (Figure 4e). Although it is difficult to distinguish these two minerals solely by XRD due to their similar structure and lattice spacings, it should be noted that the PDF-2 pattern for lithiophorite (00-041-1378) provides a better match to the experimental results.

Thermogravimetry showed that samples from Loma Caribe experience a mass loss of about 4% before 260–280 °C, probably due to the loss of adsorbed water for temperatures below 110–160 °C [33,34] and to the transformation of gibbsite to boehmite, which is reported to occur at temperatures between 150 and 260 °C [34] (Figure 5a). Between 260 and 320 °C, the mass loss is between 5 and 8%. The latter process can be ascribed to the loss of the $OH^-$ groups in the reaction from goethite to hematite (Figure 5a). This reaction (i.e., $2FeOOH \rightarrow Fe_2O_3 + H_2O$) occurs at temperatures between 300 and 344 °C [35] or 270 and 330 °C [36], and it is commonly associated with a mass loss of 10% or less if there are secondary phases. This mass loss coincides with an endothermic peak around 325 °C in the DTA curve (Figure 5b) that is considered as the result of the breakdown of goethite [34–36].

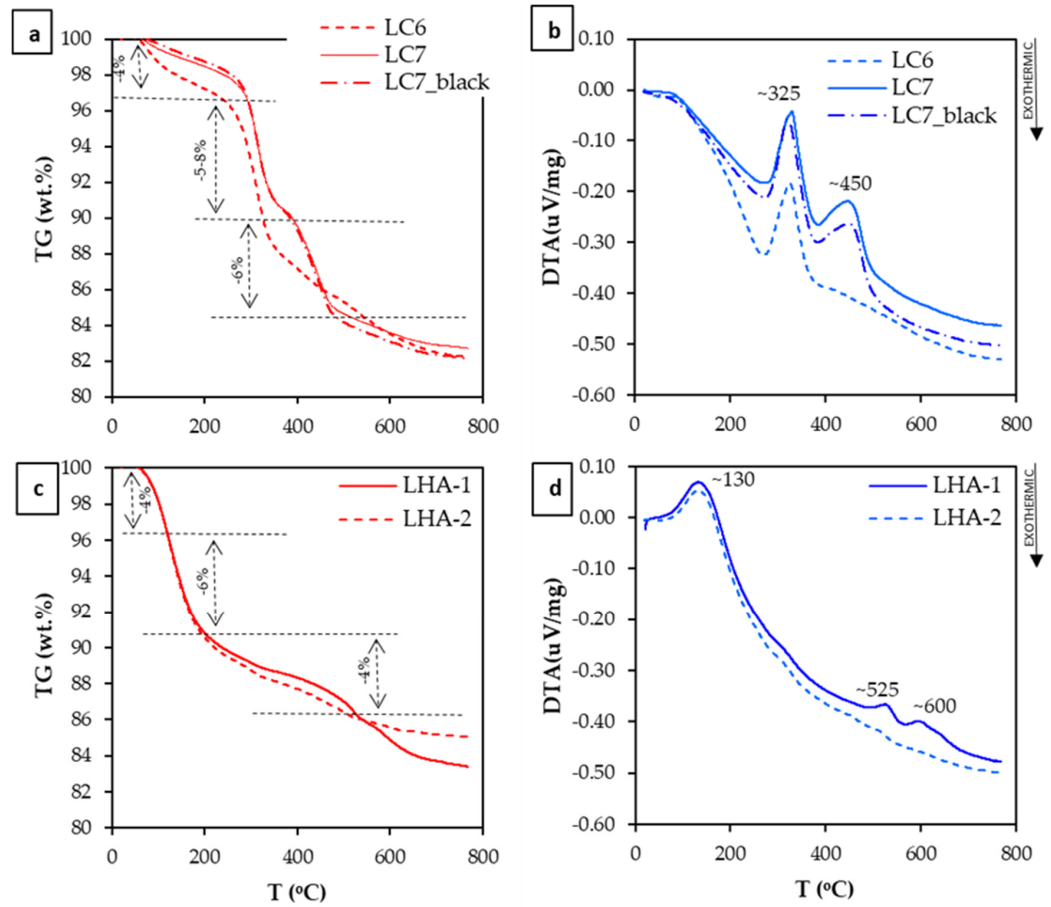


**Figure 5.** TG and DTA curves of samples LC6, LC7 and LC7_black from Loma Caribe deposit (**a**,**b**), and of samples LHA-1 and LHA-2 from Loma de Hierro (**c**,**d**).

Differential thermal analyses of samples LC7 and LC7_black revealed an additional endothermic peak at T~450 °C, associated with a mass loss of ~6%. This peak can be attributed to the dehydroxylation of AlOOH ($AlOOH \rightarrow Al_2O_3 + H_2O$) (even though it was not detected by XRD) or of an amorphous Al-hydroxide, that may occur between 450–600 °C

and 400–500 °C, respectively, or to the loss of OH in lithiophorite (430–500 °C) [37]. Llorca and co-authors [38] also measured an endothermic peak around 420–460 °C in samples of asbolane, lithiophorite and asbolane–lithiophorite intermediates of New Caledonia that was attributed to the loss of hydroxyl groups.

Samples LHA-1 and LHA-2 from Loma de Hierro showed distinctive TG and DTA analyses, compared with those of Loma Caribe (Figure 5c,d). Specifically, an endothermic peak at ~130 °C, associated with a mass loss around 10% (sample LHA-1), as well as two minor peaks around 525 and 600 °C could be distinguished. The peak at 130 °C was due to the loss of adsorbed water from clays such as smectite [37], although [39] indicated that it could also be attributed to one of the endothermic reactions shown by asbolane. Peaks at 525 and 600°C could be associated with asbolane (570–625 °C) [38]. However, research by Medeiros Ribeiro and co-authors [39] suggests that the peak around 600 °C refers to the dehydroxylation of the interlayer hydroxide of chlorite.

Depending on the crystallinity of Mn-oxyhydroxides, the characteristic IR frequencies appeared as a single broad band, or in distinct bands in the range of 425–530 $cm^{-1}$ (associated with Mn–O bonds of the $MnO_6$ octahedra) and in the range of 3100–3500 $cm^{-1}$ (stretching modes of OH groups) [40,41]. The band around 1600 $cm^{-1}$ was the water bending mode, that may suggest that at least some of the OH is $H_2O$ [41,42]. According to IR spectra (Figure 6), samples were mostly poorly crystalline, although peaks around 3400, 1600 and 1000 $cm^{-1}$ could be assigned to lithiophorite, while those around 3600–3500 $cm^{-1}$ were related to gibbsite [43,44]. The shadowed area (800–600 $cm^{-1}$) in samples LHA-1 and LHA-2 included some peaks related to Mn-oxides and clays [45], and the peak around 1200 $cm^{-1}$ could be related to kaolinite. It must be noted that mineral contamination can also affect IR spectra.

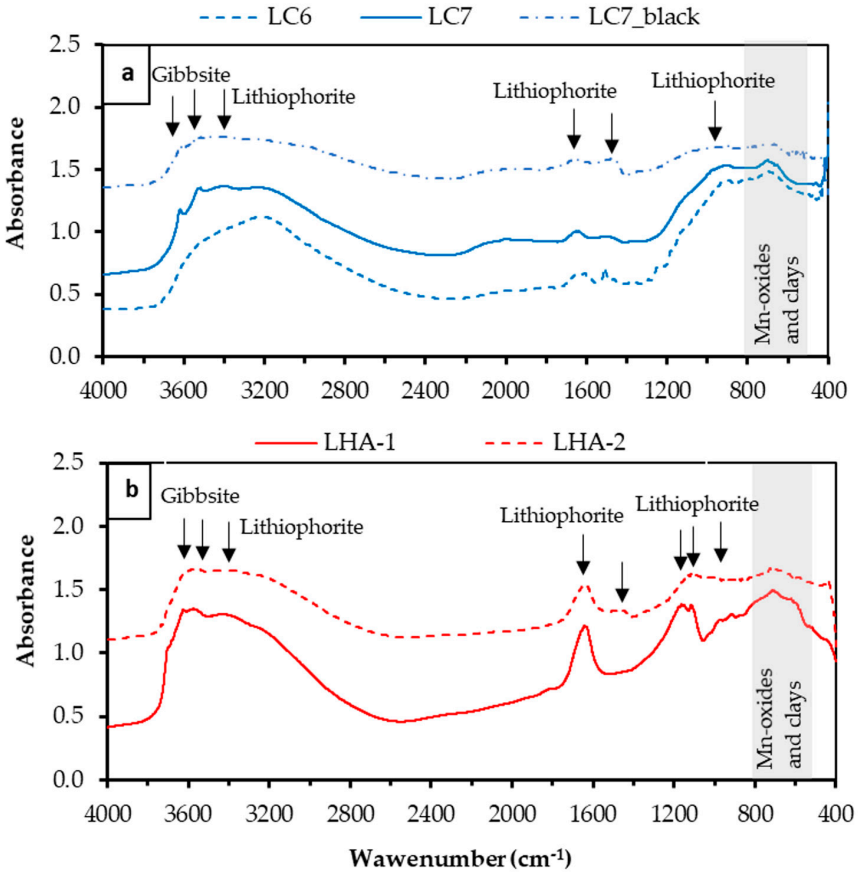


**Figure 6.** IR spectra of (**a**) samples LC6, LC7 and LC7_black from Loma Caribe (Dominican Republic), and (**b**) samples LHA-1and LHA-2 from Loma de Hierro (Venezuela). Arrows indicate the peak positions. The grey shadowed band represents the peaks associated with Mn-oxides.

### *4.2. Co-Mn Mineralisations*

#### 4.2.1. Mn-Oxyhydroxides

In the Loma Caribe samples, Co-rich Mn-oxyhydroxides were in close association with Fe–Al-oxyhydroxides. Three major textural types were identified.

The first type was characterised by banded and colloform aggregates (Figure 7), which is the most common texture observed in Mn-oxyhydroxides. Some bands within the colloform aggregates appeared to be formed by parallel and/or radial fibrous aggregates (Figure 7a–c). Figure 8 shows the spatial distribution of some elements within these colloform aggregates and fibrous bands. In general, a close spatial association between Mn, Ni, Co and Al was observed, while, conversely, Si had a mirrored distribution, and no significant variations of Fe or Mg were observed. Colloform aggregates locally displayed distinct external rims (Figure 7a) and in rare occasions, these particles had a uniform core (Figure 7c).

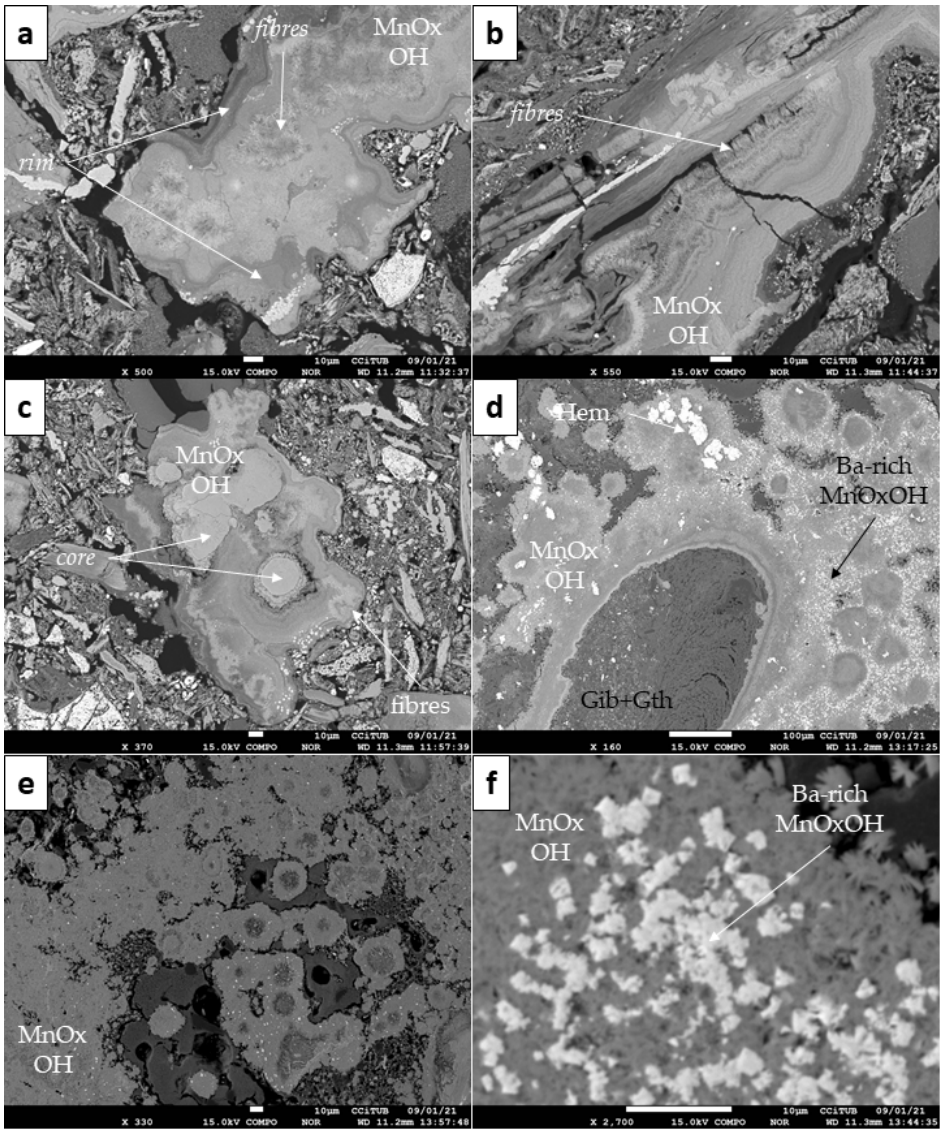


**Figure 7.** Back-scattered electron (BSE) photomicrographs of the Mn-oxyhydroxide textures identified in Loma Caribe (Dominican Republic) samples: (**a**–**c**) colloform aggregates including distinct features (rims, core and fibres; see text for explanation); (**d**,**e**) globular spherulitic aggregates with a gibbsite and goethite (Gib + Gth) core (**d**), and as small, isolated spherulitic aggregate particles (**e**); (**f**) Ba-rich angular grains within the globular spherulitic aggregates. Note the flaky appearance of the Mn-oxyhydroxides in the background in (**f**).

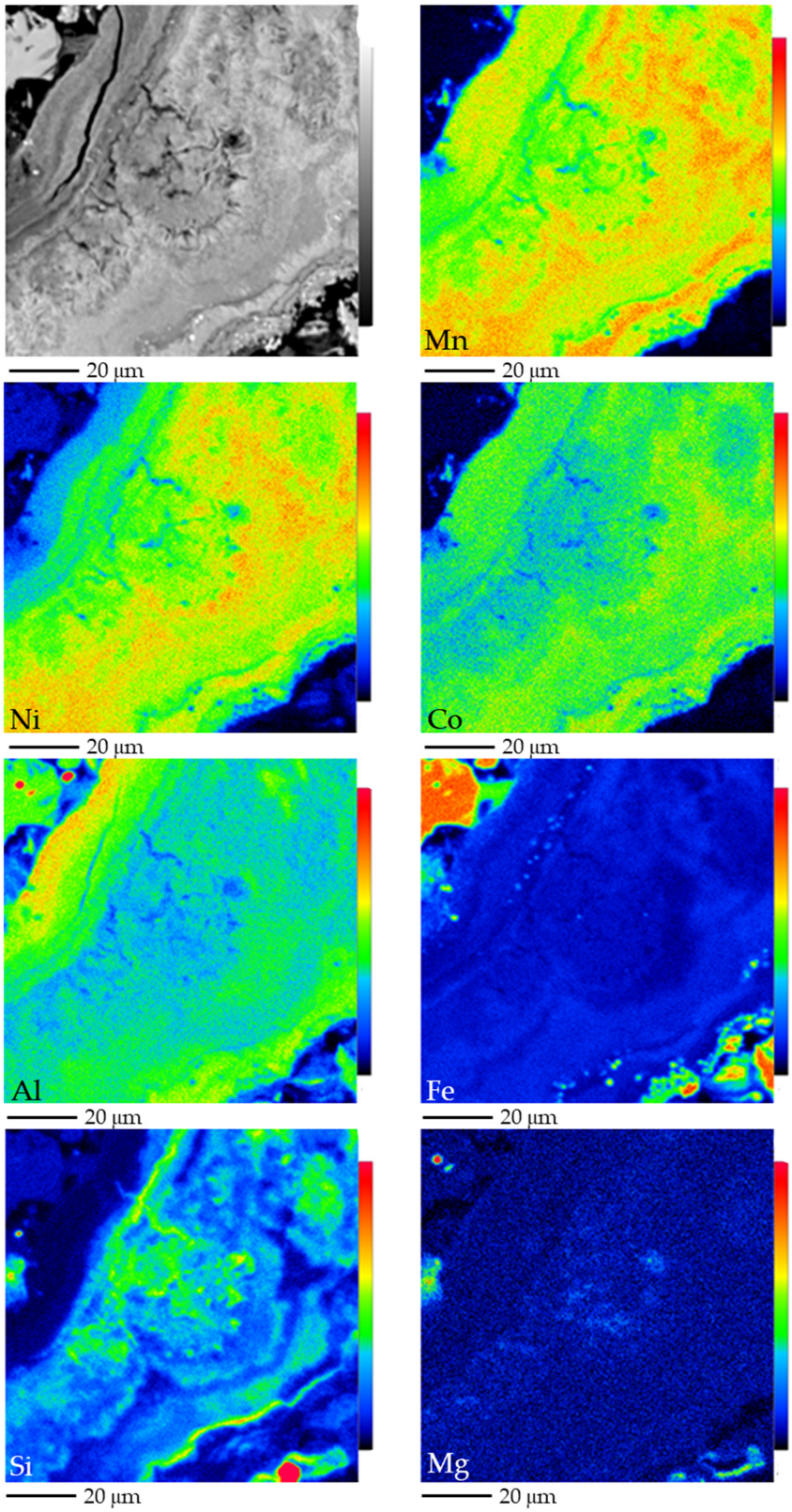


**Figure 8.** BSE photomicrograph (top left) and Mn, Ni, Co, Al, Fe, Si and Mg X-ray elemental maps obtained by EMPA of banded colloform aggregates from Loma Caribe. Colour scale from black to red indicates increasing element content.

The second Mn-oxyhydroxide type was slightly less abundant, and consisted of globular to spherulitic aggregates, with sizes from some tens to several hundreds of micrometres;

locally, larger aggregates appeared to be hollow-cored, filled with goethite and/or gibbsite (Figure 7d,e). These globular to spherulitic aggregates were composed of short, flaky crystals (Figure 7f). The least abundant occurrences were discrete, micrometre-sized, Ba-rich angular grains (with high mean atomic number Z in BSE images, Figure 7d,f) disseminated within some globular-spherulitic aggregates (of lower mean atomic number Z). These last two types were only observed in the saprolite horizon sample.

In Loma de Hierro (Venezuela), Mn-oxyhydroxide grains are a minor component of the mineralogical assemblage. According to their textural features, three types were identified (Figure 9). Firstly, as in Loma Caribe, they typically displayed banded colloform features, as kidney-shaped (Figure 9a), elongated (Figure 9b), and sub-rounded (Figure 9c,d) grains, measuring a few hundreds of micrometres in diameter or length, surrounded by goethite and other oxides. Certain rounded grains displayed one or more concentric rims having an homogeneous compositional footprint (Figure 9c,d). Locally, Ni and Co were concentrated in the outer rims, while the Mn grade was higher in the core (Figure 10).

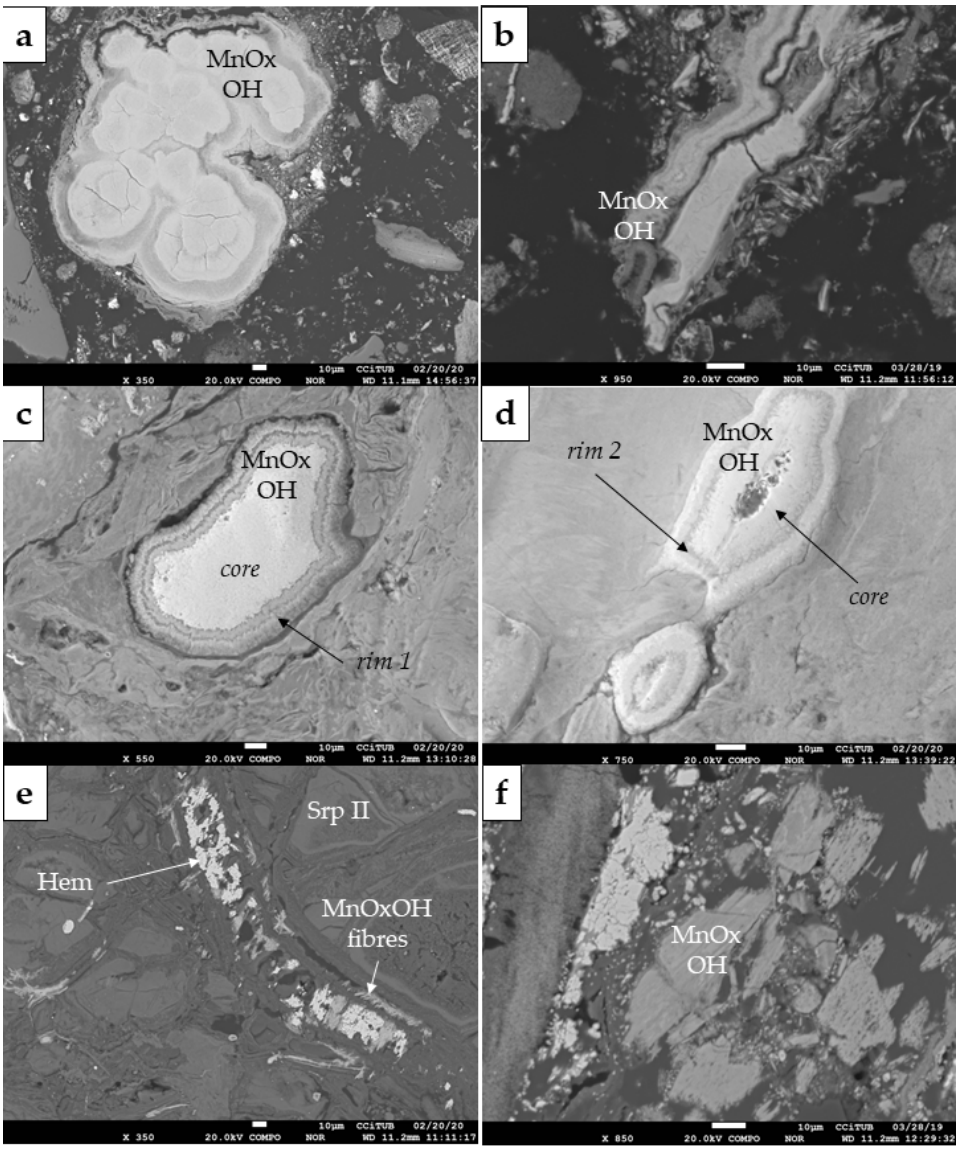


**Figure 9.** BSE photomicrographs of the textural features displayed by Mn-oxyhydroxides in Loma de Hierro Ni laterites (Venezuela): (**a**–**d**) colloform aggregates developing kidney-shaped grains (**a**), elongated grains (**b**), and sub-rounded individual grains with distinct multi-phase rims (**c**,**d**); (**e**) fibres within veinlets, coexisting with hematite (Hem) and secondary serpentine (Serp-II); (**f**) fragmented tabular aggregates.

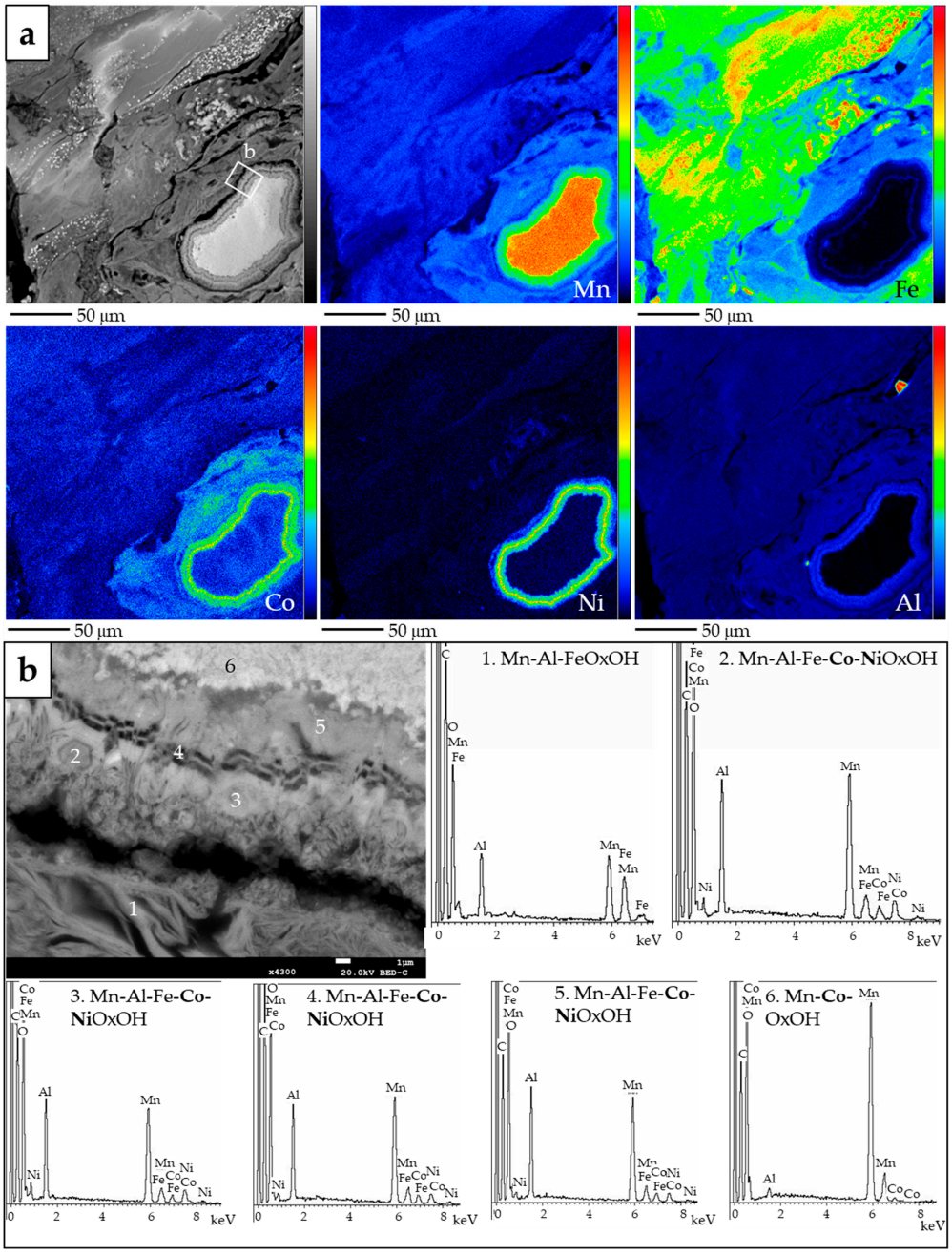


**Figure 10.** (**a**) BSE photomicrograph (top left) and Mn, Fe, Co, Ni and Al X-ray elemental maps obtained by EMPA, of the same sub-rounded multi-phase Mn-oxyhydroxide grain in Figure 9c (Loma de Hierro), in a matrix of Mn- and Fe-oxyhydroxides (colour scale from black to red indicates increasing element content); (**b**) magnified image of the outer rim of the same grain, displaying variations in composition in terms of Mn, Al, Fe, Ni and Co.

The second type, less common, were short fibres of a few tens of micrometres in length, in close association with Fe-oxide and within serpentine veinlets (Figure 9e).

Finally, the least common Mn-oxyhydroxide in Loma de Hierro occurred as fragmented tabular aggregates, dispersed in the goethite matrix (Figure 9f).

With regard to the chemical composition of Loma Caribe Mn-oxyhydroxides, colloform aggregates and rims, fibrous bands and globular spherulitic aggregates showed high variations in MnO (14–34 wt.%), NiO (4–21 wt.%), CoO (4–12 wt.%), $SiO_2$ (0.4–11 wt.%), $Al_2O_3$ (7–22 wt.%) and FeO (< 9 wt.%). However, the uniform cores within the colloform aggregates had a considerably higher amount of MnO (average of 54 wt.%) while CoO,

FeO, $Al_2O_3$, and $SiO_2$ contents were below 1 wt.%, and Ni content was close to 4 wt.% NiO. The angular, high-Z grains were characterised by high Ba and Mn contents (10–11 wt.% BaO and 54–59 wt.% MnO) and low amounts of Ni and Co (0.7 wt.% NiO, 1 wt.% CoO) (Table 1).

In Loma de Hierro, the MnO content in the colloform and tabular aggregates varied from 20 to 41 wt.%. They contained 2–12 wt.% $Al_2O_3$, 2 -28 wt.% FeO, 8–20 wt.% NiO, 3–7 wt.% CoO, <2 wt.% $SiO_2$, and <5 wt.% MgO (Table 2). However, grain cores were richer in Mn (76–80 wt.% MnO) but were Ni and Co poor (<0.3 wt.% NiO and <2 wt.% CoO). These cores were overgrown by a rim with high Al (12–15 wt.%) and relatively low Mn (29–37 wt.%) (Table 2; Figure 9c), or another with high Mn (71–73 wt.%) and low Al (2–3 wt.% $Al_2O_3$) (Table 2; Figure 9d). The short fibres had Mn, Fe, Mg, Co and Ni values similar to those of colloform and tabular aggregates, but were richer in Si (up to 14 wt.% $SiO_2$, partly probably due to contamination of the analyses) (Table 2).

Most of the compositional analyses of Mn-oxyhydroxides had a Mn content within 20 and 40 wt.% Mn, with contents of Ni and Co up to 16 and 10 wt.%, respectively. Some analyses from the Mn–Co rich zone (sample LHA) were the richest in Mn content (~60 wt.% of Mn) although they showed very low Ni and Co contents (Figure 11).

In general, samples from Loma de Hierro were richer in Mn than those of Loma Caribe (Figure 11a,b). Both sets of samples showed similar Ni contents but those of Loma Caribe were found to be Co richer. A common feature observed in all samples was a positive correlation between Co and Al contents (Figure 11c).

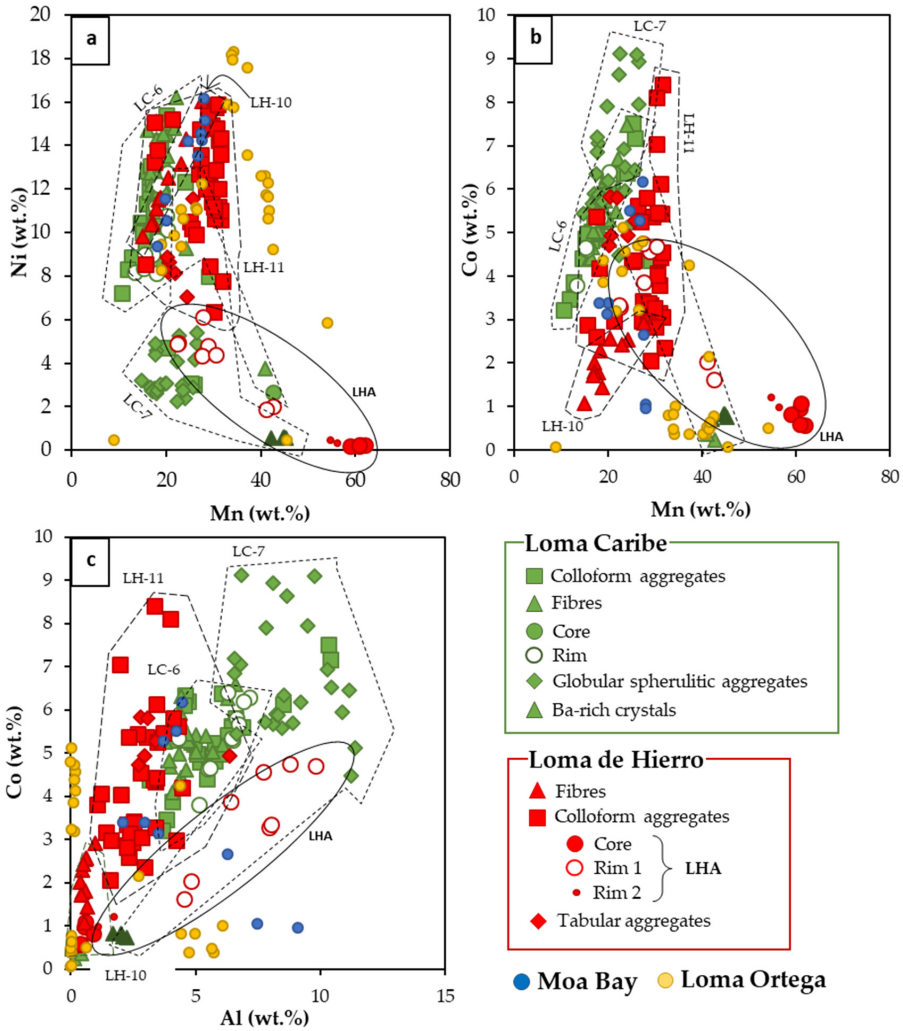


**Figure 11.** Binary diagrams of (**a**) Ni vs. Mn, (**b**) Co vs. Mn, and (**c**) Co vs. Al (in wt.%), of the Mn–Co minerals analysed in this study, and from Loma Ortega [46] and Moa Bay [47].

**Table 1.** Representative EMP analyses (in weight percent) of the studied Co–Mn-oxyhydroxide types in Loma Caribe (Dominican Republic). <d.l.: below detection limit; n.a: not analysed; F: fibres; CA: colloform aggregates; C: core; R: rim; GS: globular spherulitic aggregates; Ba: Ba-rich minerals.

| Label | Texture | $SiO_2$ | $Al_2O_3$ | CaO | $K_2O$ | $Na_2O$ | MgO | NiO | CoO | FeO | MnO | $Cr_2O_3$ | BaO | $TiO_2$ | $V_2O_3$ | $Sc_2O_3$ | Total |
|---|---|---|---|---|---|---|---|---|---|---|---|---|---|---|---|---|---|
| LC-6_01 | F | 6.24 | 8.37 | 0.04 | <0.01 | 0.01 | 0.37 | 17.22 | 6.73 | 6.84 | 26.01 | <0.01 | 0.01 | n.a | n.a | n.a | 71.84 |
| LC-6_02 | F | 3.01 | 8.18 | 0.05 | 0.04 | 0.09 | 0.37 | 18.82 | 6.96 | 7.82 | 27.90 | <d.l. | 0.11 | n.a | n.a | n.a | 73.34 |
| LC-6_03 | F | 3.99 | 8.71 | 0.03 | 0.03 | 0.01 | 0.12 | 20.60 | 8.52 | 8.72 | 28.63 | 0.03 | <d.l. | n.a | n.a | n.a | 79.38 |
| LC-6_04 | F | 4.14 | 9.47 | 0.02 | 0.02 | 0.03 | 0.24 | 14.97 | 6.89 | 9.32 | 23.57 | 0.05 | 0.04 | n.a | n.a | n.a | 68.75 |
| LC-6_05 | F | 2.09 | 9.50 | 0.07 | <0.01 | 0.02 | 0.13 | 19.23 | 6.38 | 6.21 | 23.09 | 0.03 | 0.02 | n.a | n.a | n.a | 66.76 |
| LC-7_01 | F | 0.49 | 12.47 | 0.02 | 0.17 | 0.61 | 0.64 | 11.82 | 9.51 | 4.02 | 31.08 | <d.l. | <d.l. | n.a | n.a | n.a | 70.82 |
| LC-6_06 | CA | 4.36 | 8.91 | 0.06 | <0.01 | 0.01 | 0.11 | 19.11 | 7.88 | 8.72 | 26.86 | <0.01 | <d.l. | n.a | n.a | n.a | 76.02 |
| LC-6_07 | CA | 6.65 | 10.47 | 0.04 | <0.01 | 0.06 | 0.08 | 16.32 | 6.12 | 7.47 | 20.68 | <d.l. | 0.09 | n.a | n.a | n.a | 67.98 |
| LC-6_08 | CA | 1.40 | 10.73 | 0.03 | 0.02 | 0.06 | 0.07 | 16.63 | 6.30 | 6.45 | 21.62 | 0.03 | 0.09 | n.a | n.a | n.a | 63.43 |
| LC-6_09 | CA | 7.70 | 10.91 | 0.05 | 0.02 | 0.18 | 0.15 | 13.95 | 6.64 | 5.79 | 22.35 | 0.02 | 0.08 | n.a | n.a | n.a | 67.86 |
| LC-7_02 | CA | 0.39 | 5.95 | 0.11 | 0.43 | 1.13 | 2.02 | 10.20 | 5.56 | 6.24 | 37.47 | 0.02 | 0.42 | n.a | n.a | n.a | 69.94 |
| LC-7_03 | CA | 1.09 | 11.39 | 0.04 | 0.16 | 0.46 | 0.35 | 15.70 | 8.11 | 3.72 | 30.91 | <0.01 | <d.l. | n.a | n.a | n.a | 71.93 |
| LC-7_04 | CA | 1.91 | 16.03 | 0.05 | 0.14 | 0.37 | 0.05 | 6.01 | 7.79 | 12.62 | 25.95 | 0.05 | <d.l. | n.a | n.a | n.a | 70.97 |
| LC-7_05 | CA | 0.50 | 19.67 | 0.04 | 0.05 | 0.18 | 0.02 | 3.85 | 9.12 | 4.08 | 33.27 | 0.10 | <d.l. | n.a | n.a | n.a | 70.87 |
| LC-6_10 | C | 0.39 | 0.24 | 0.03 | 0.03 | 0.04 | 7.78 | 3.36 | 0.30 | 0.63 | 55.20 | <d.l. | 0.66 | n.a | n.a | n.a | 68.66 |
| LC-6_11 | C | 0.61 | 0.76 | 0.04 | 0.05 | 0.04 | 6.65 | 4.76 | 0.46 | 0.91 | 52.85 | <d.l. | 0.57 | n.a | n.a | n.a | 67.71 |
| LC-6_12 | R | 11.27 | 10.38 | 0.09 | 0.03 | 0.16 | 0.11 | 11.43 | 5.88 | 5.13 | 19.96 | 0.02 | <d.l. | n.a | n.a | n.a | 64.46 |
| LC-6_13 | R | 1.52 | 9.69 | <d.l. | 0.03 | 0.06 | 0.07 | 10.41 | 4.83 | 7.46 | 17.20 | 0.04 | 0.06 | n.a | n.a | n.a | 51.38 |
| LC-6_14 | R | 2.11 | 8.16 | 0.10 | <0.01 | <d.l. | 0.21 | 15.53 | 6.81 | 8.13 | 23.74 | <d.l. | <d.l. | n.a | n.a | n.a | 64.79 |
| LC-6_15 | R | 1.56 | 13.53 | 0.04 | 0.03 | 0.08 | 0.11 | 13.74 | 7.99 | 4.58 | 25.72 | 0.02 | <d.l. | n.a | n.a | n.a | 67.40 |
| LC-6_16 | R | 7.92 | 12.20 | 0.18 | 0.04 | 0.19 | 0.11 | 14.23 | 6.80 | 6.49 | 22.84 | <d.l. | <d.l. | n.a | n.a | n.a | 71.00 |
| LC-6_17 | R | 1.34 | 11.85 | 0.09 | 0.04 | 0.04 | 0.25 | 16.23 | 8.13 | 4.91 | 26.05 | 0.02 | <d.l. | n.a | n.a | n.a | 68.95 |
| LC-7_06 | GS | 0.26 | 15.33 | 0.07 | 0.11 | 0.24 | 0.16 | 6.85 | 11.36 | 1.90 | 34.17 | 0.02 | 0.33 | n.a | n.a | n.a | 70.81 |
| LC-7_07 | GS | 3.40 | 12.39 | 0.31 | 0.05 | 0.49 | 0.24 | 5.60 | 8.71 | 11.08 | 22.74 | 0.65 | 0.06 | n.a | n.a | n.a | 65.71 |
| LC-7_08 | GS | 5.46 | 16.01 | 0.14 | 0.12 | 0.37 | 0.11 | 3.48 | 7.10 | 13.70 | 21.66 | 0.86 | 0.02 | n.a | n.a | n.a | 69.03 |
| LC-7_09 | GS | 2.63 | 14.82 | 0.13 | 0.07 | 0.18 | 0.08 | 3.90 | 10.04 | 8.30 | 25.64 | 0.26 | <d.l. | n.a | n.a | n.a | 66.05 |
| LC-7_10 | GS | 7.29 | 15.57 | 0.17 | 0.10 | 0.32 | 0.10 | 3.43 | 7.49 | 9.97 | 22.02 | 0.39 | <d.l. | n.a | n.a | n.a | 66.84 |
| LC-7_11 | GS | 1.73 | 19.73 | 0.06 | 0.05 | 0.13 | 0.05 | 3.58 | 8.29 | 6.69 | 30.43 | 0.19 | <d.l. | n.a | n.a | n.a | 70.92 |
| LC-7_12 | GS | 0.98 | 21.11 | 0.02 | <0.01 | 0.09 | 0.02 | 3.69 | 8.20 | 2.89 | 33.13 | 0.05 | 0.09 | n.a | n.a | n.a | 70.26 |
| LC-7_13 | GS | 1.69 | 21.26 | 0.02 | 0.01 | 0.09 | 0.04 | 2.85 | 5.70 | 10.58 | 28.71 | 0.18 | 0.10 | n.a | n.a | n.a | 71.23 |
| LC-7_14 | Ba | 0.30 | 3.91 | 0.04 | 0.51 | 0.36 | 0.05 | 0.70 | 0.96 | 2.75 | 58.51 | 0.08 | 9.87 | n.a | n.a | n.a | 78.04 |
| LC-7_15 | Ba | 0.25 | 3.20 | 0.05 | 0.51 | 0.29 | 0.02 | 0.74 | 1.04 | 3.16 | 57.82 | 0.10 | 10.51 | n.a | n.a | n.a | 77.70 |
| LC-7_16 | Ba | 0.27 | 3.81 | <0.01 | 0.41 | 0.27 | 0.03 | 0.71 | 1.04 | 2.79 | 57.63 | 0.07 | 10.56 | n.a | n.a | n.a | 77.59 |
| LC-7_17 | Ba | 0.47 | 4.21 | <d.l. | 0.43 | 0.26 | 0.02 | 0.71 | 0.91 | 6.33 | 54.30 | 0.17 | 10.51 | n.a | n.a | n.a | 78.32 |

**Table 2.** Representative EMP analyses (in weight percent) of the studied Co–Mn-oxyhydroxide types in Loma de Hierro (Venezuela). <d.l.: below detection limit; F-fibres; CA–colloform aggregates; C-core; R-rim; T-tabular.

| Label | Texture | $SiO_2$ | $Al_2O_3$ | CaO | $K_2O$ | $Na_2O$ | MgO | NiO | CoO | FeO | MnO | $Cr_2O_3$ | BaO | $TiO_2$ | $V_2O_3$ | $Sc_2O_3$ | Total |
|---|---|---|---|---|---|---|---|---|---|---|---|---|---|---|---|---|---|
| LH-10_01 | F | 3.47 | 1.06 | 0.03 | 0.04 | 0.01 | 4.60 | 18.19 | 3.23 | 12.48 | 31.30 | 0.03 | 0.05 | n.a. | n.a. | n.a. | 74.50 |
| LH-10_02 | F | 3.93 | 1.81 | 0.08 | 0.02 | 0.04 | 6.29 | 20.40 | 3.71 | 3.87 | 35.48 | <d.l. | 0.24 | n.a. | n.a. | n.a. | 75.86 |
| LH-10_03 | F | 5.56 | 0.82 | 0.06 | 0.06 | <d.l. | 6.16 | 13.20 | 2.19 | 24.20 | 21.70 | <d.l. | n.a. | <0.01 | <d.l. | n.a. | 73.94 |
| LH-10_04 | F | 4.75 | 0.98 | 0.07 | 0.04 | 0.06 | 5.80 | 16.76 | 3.08 | 12.47 | 29.73 | <d.l. | n.a. | 0.02 | <0.01 | n.a. | 73.76 |
| LH-11_01 | CA | 0.12 | 2.01 | 0.08 | n.a. | n.a. | 3.12 | 18.77 | 3.78 | 9.96 | 40.03 | <d.l. | n.a. | 0.01 | 0.02 | <d.l. | 77.90 |
| LH-11_02 | CA | 0.20 | 2.26 | 0.05 | n.a. | n.a. | 3.48 | 18.15 | 4.83 | 10.12 | 39.41 | <d.l. | n.a. | <d.l. | <d.l. | <d.l. | 78.50 |
| LH-11_03 | CA | 0.13 | 2.68 | 0.06 | n.a. | n.a. | 2.07 | 20.02 | 5.17 | 8.90 | 38.13 | <d.l. | n.a. | <d.l. | <d.l. | <d.l. | 77.16 |
| LH-11_04 | CA | 0.16 | 2.98 | 0.04 | n.a. | n.a. | 4.26 | 13.52 | 8.95 | 8.96 | 37.55 | <d.l. | n.a. | <d.l. | 0.01 | <d.l. | 76.44 |
| LH-11_05 | CA | 0.37 | 6.35 | 0.04 | n.a. | n.a. | 3.76 | 16.23 | 7.37 | 4.21 | 40.69 | <d.l. | n.a. | <d.l. | n.a. | <d.l. | 79.02 |
| LH-11_06 | CA | 0.30 | 7.53 | 0.03 | n.a. | n.a. | 4.51 | 13.98 | 10.70 | 2.08 | 39.03 | <d.l. | n.a. | <d.l. | <0.01 | <d.l. | 78.16 |
| LHA_1 | C | 0.04 | 1.02 | 0.02 | 0.12 | <d.l. | <d.l. | 0.27 | 1.23 | 0.45 | 78.56 | <d.l. | 0.12 | n.a. | n.a. | n.a. | 81.82 |
| LHA_2 | C | 0.13 | 1.72 | <0.01 | 0.15 | 0.08 | 0.05 | 0.25 | 1.05 | 1.62 | 75.97 | 0.01 | 0.26 | n.a. | n.a. | n.a. | 81.30 |
| LHA_3 | C | 0.05 | 1.06 | <0.01 | 0.08 | <d.l. | <0.01 | 0.30 | 1.38 | 0.45 | 78.74 | 0.02 | 0.07 | n.a. | n.a. | n.a. | 82.15 |
| LHA_4 | R | 0.08 | 8.58 | <0.01 | 0.16 | 0.07 | 0.03 | 2.54 | 2.06 | 3.05 | 54.91 | 0.03 | 0.50 | n.a. | n.a. | n.a. | 72.02 |
| LHA_5 | R | 0.13 | 9.13 | 0.03 | 0.22 | <d.l. | 0.10 | 2.37 | 2.59 | 3.55 | 52.98 | <d.l. | 0.72 | n.a. | n.a. | n.a. | 71.81 |
| LHA_6 | R | 0.08 | 18.56 | <d.l. | 0.08 | 0.10 | 0.04 | 5.61 | 5.97 | 1.47 | 39.21 | <d.l. | 0.12 | n.a. | n.a. | n.a. | 71.24 |
| LHA_7 | R | 0.09 | 2.10 | 0.02 | 0.59 | 0.09 | 0.03 | 0.37 | 1.25 | 0.49 | 72.74 | <d.l. | 1.30 | n.a. | n.a. | n.a. | 79.07 |
| LHA_8 | R | 0.09 | 3.26 | 0.04 | 0.90 | 0.05 | 0.02 | 0.57 | 1.55 | 0.56 | 70.65 | 0.01 | 1.31 | n.a. | n.a. | n.a. | 79.01 |
| LH-11_07 | T | 1.41 | 5.25 | 0.04 | n.a. | n.a. | 2.50 | 10.43 | 7.42 | 24.66 | 26.30 | 0.80 | n.a. | 0.04 | 0.03 | <d.l. | 78.88 |
| LH-11_08 | T | 1.19 | 5.79 | 0.02 | n.a. | n.a. | 2.45 | 10.36 | 7.38 | 22.38 | 28.17 | 0.66 | n.a. | 0.02 | 0.03 | <d.l. | 78.44 |
| LH-11_09 | T | 0.92 | 6.43 | 0.02 | n.a. | n.a. | 2.72 | 14.72 | 6.72 | 17.50 | 33.08 | 0.46 | n.a. | 0.02 | 0.02 | <d.l. | 82.61 |
| LH-11_10 | T | 1.35 | 5.15 | 0.03 | n.a. | n.a. | 2.74 | 11.27 | 6.00 | 28.23 | 26.08 | 0.69 | n.a. | 0.04 | 0.04 | <d.l. | 81.62 |

4.2.2. Mn-Bearing Phyllosilicates

In addition, Co was identified in the phyllosilicates of Loma de Hierro. According to XRPD, the clay component was dominated by chlorite and smectite. These clay species occurred as micrometre-sized platy individual crystals (Figure 12). In some cases, an inner core with lower Z, and an outer rim with higher Z was distinguished (in BSE photomicrographs, Figure 12). The core contained 27–34 wt.% $SiO_2$, 25–29 wt.% $Al_2O_3$, <2 wt.% FeO, 6–12 wt.% MnO, <0.5 wt.% NiO, and 2–4 wt.% CoO (Table 3). The rim yielded 19–20 wt.% $SiO_2$, 23–24 wt.% $Al_2O_3$, 3–4 wt.% FeO, 18–19 wt.% MnO, <0.9 wt.% NiO, and 6–7 wt.% CoO. Interestingly, both contained <1 wt.% MgO (Figure 12).

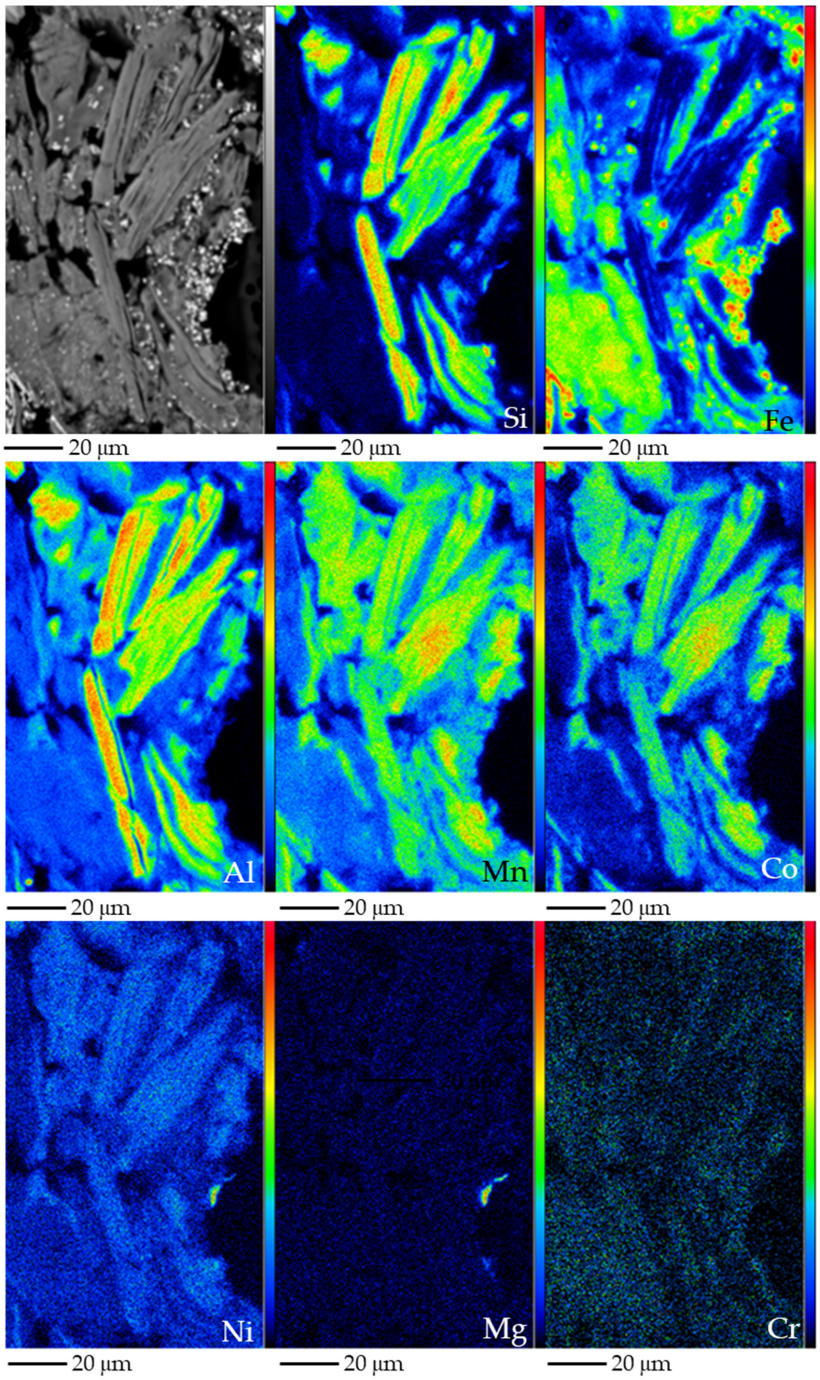


**Figure 12.** BSE photomicrograph of sample LHA (top left), and Si, Fe, Al, Mn, Co, Ni, Mg and Cr X-ray elemental maps obtained by EMPA, of an aggregate of Mn–Ni–Co-bearing chlorite. Colour scale from black to red indicates increasing element content.

**Table 3.** Representative EMP analyses (in weight percent) of the studied Co-bearing phyllosilicates from Loma de Hierro (Venezuela). <d.l.: below detection limit; C-core; R-rim.

| Label | Texture | $SiO_2$ | $Al_2O_3$ | CaO | $K_2O$ | $Na_2O$ | MgO | NiO | CoO | FeO | MnO | $Cr_2O_3$ | BaO | Total |
|---|---|---|---|---|---|---|---|---|---|---|---|---|---|---|
| LHA_10 | C | 34.35 | 28.60 | 0.06 | 0.06 | 0.00 | 0.08 | 0.30 | 1.54 | 1.13 | 5.78 | 0.04 | <d.l. | 71.95 |
| LHA_11 | C | 26.50 | 24.96 | 0.03 | 0.04 | 0.06 | 0.04 | 0.54 | 3.95 | 1.49 | 12.08 | <d.l. | 0.04 | 69.73 |
| LHA_12 | R | 19.91 | 24.12 | 0.04 | 0.13 | 0.02 | 0.01 | 0.86 | 5.93 | 3.29 | 18.22 | 0.02 | 0.02 | 72.57 |
| LHA_13 | R | 18.76 | 23.36 | 0.03 | 0.06 | <d.l. | 0.02 | 0.79 | 6.53 | 3.41 | 18.95 | <d.l. | 0.05 | 71.96 |

## 5. Discussion

### *5.1. Co-Mn Bearing Minerals in Loma Caribe and Loma de Hierro*

Most of the Loma Caribe and Loma de Hierro Mn-bearing minerals from the oxide horizon had a composition between Ni asbolane ($(Ni,Co)_xMn(O,OH)_4 \cdot nH_2O$) and lithiophorite ($(Al,Li)MnO_2(OH)_2$) (Figure 13). These minerals mainly formed colloform to tabular textures in the case of Loma de Hierro, while in Loma Caribe they were also present as fibrous aggregates. The purest Ni asbolane was found in sample LH-10 of Loma de Hierro. However, in the saprolite horizon of Loma Caribe, Mn-bearing minerals were mainly globular or spherulitic lithiophorites. These observations were consistent with the results of DRX, DTA-TG and FTIR, which clearly indicated the occurrence of lithiophorite in sample LC-7.

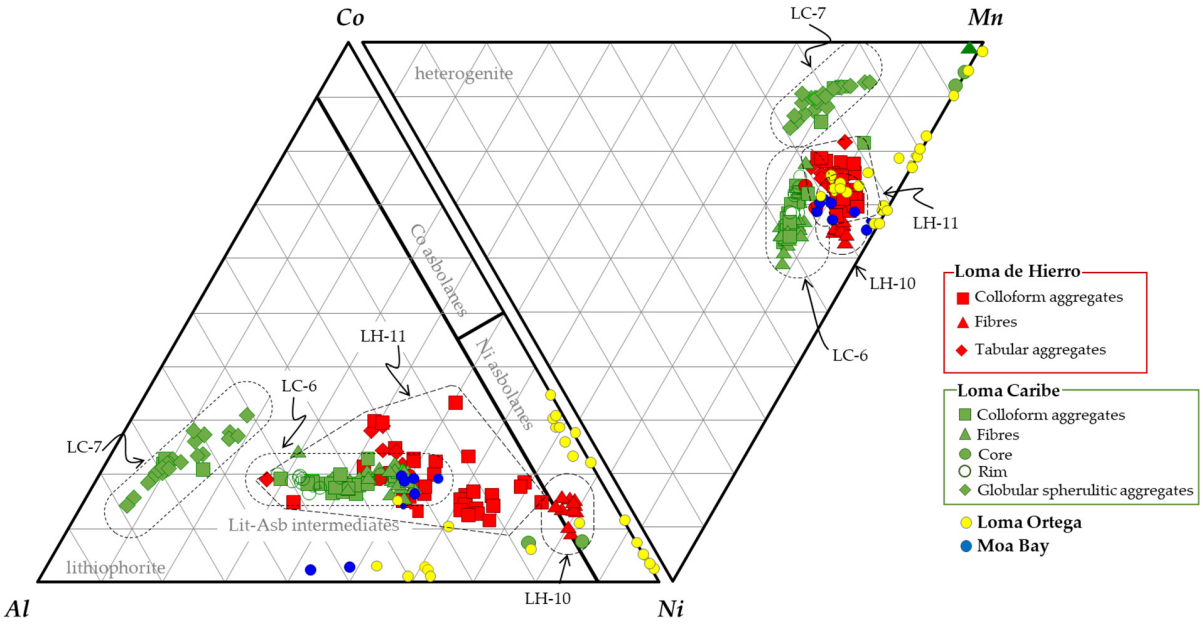


**Figure 13.** Ternary plots representing Mn, Ni, Co, Al contents (cation proportions calculated on the basis of 100 oxygens) obtained from EMPA analyses on Mn-oxyhydroxides (lithiophorites, lithiophorite–asbolane intermediates and asbolane) from Loma Caribe and Loma de Hierro (this study), Loma Ortega [46] and Moa Bay [47].

The highest Mn contents were found in sample LHA, from Loma de Hierro. They were explained by the abundance of grains with a core rich in Mn (up to 80 wt.% MnO, Table 2), but poor in Co and Ni. Hence, these were not considered lithiophorite nor lithiophorite–asbolane intermediates. These grains were surrounded by rims with alternate Mn-rich or Co/Ni-rich compositions.

Putzolu and and co-authors [15] described two different generations of romanèchite, which despite their close paragenetic association, showed different chemical compositions. Romanèchite I had an average BaO content of 7.64 wt.%, with low amounts of NiO and CoO (average values of 1.21 and 0.72 wt.%, respectively), while romanèchite II had lower BaO (average 2.68 wt.%) and higher NiO and CoO (average values of 2.90 and 1.48 wt.%, respectively). Ba-rich Mn-oxyhydroxides identified in Loma Caribe (Figure 7f) presented

slightly higher BaO contents (up to 10.5 wt.%, Table 1, Figure 7f) than those of romanèchite I of [15], although NiO and CoO contents were lower (less than 0.7 and 1.4 wt.%, respectively). Pure romanèchite has the structural formulae $Ba_{0.66}Mn_5O_{10}{\cdot}34H_2O$, in which the content of Ba is around 20 wt.% BaO [48]. In our case, as in [15], Ba content was far below the stoichiometric value.

Furthermore, the association of Mn (and Co) with phyllosilicates (Table 3) is not uncommon, as it has also been observed in serpentine minerals [49] and smectite clays [50].

### *5.2. Comparison with Other Co-Mn Mineralisations in Lateritic Systems*

The Ni and Co of Mn-oxyhydroxides from the Loma Caribe and Loma de Hierro were similar to those of other Ni laterites of the Caribbean region. Their Ni grade was similar to that of Moa Bay, and a bit lower than that measured in Loma Ortega [46,47], however, the Co contents were considerably higher in Loma Caribe and Loma de Hierro when compared with those of Loma Ortega and Moa Bay (Figure 11a,b).

The Al content in Mn-oxyhydroxides object of this study was higher in Loma Caribe and Loma de Hierro than in Loma Ortega and Moa Bay (Figure 11c). In the hybrid hydrous Mg silicate–clay silicate type Ni laterite deposit of Loma Ortega (Falcondo mining district, Dominican Republic), Co-bearing Mn phases were observed as coatings or vein fillings, close to quartz, goethite and serpentine II, replacing pyroxene, olivine and serpentine along grain boundaries and fractures [46]. As shown in Figure 13, they were mostly Ni asbolanes with Mn and Ni contents between 11 and 70 wt.% MnO, and up to 23 wt.% NiO, respectively. In most cases, Co content was below 1 wt.% CoO, although in some cases it graded up to 6.5 wt.% CoO. Al and Fe were highly variable, ranging from 0.1 to 11.5 wt.% $Al_2O_3$ and from 0.1 to 21 wt.% FeO. In general, in these samples, the Fe and Al contents were anti-correlated. In Moa Bay, an oxide type laterite deposit in Cuba, Mn-bearing minerals, mostly lithiophorite-asbolane intermediates (Figure 13), are found as veins and coatings along fractures at the lowest part of the oxide horizon [47]. In these minerals, Mn content ranges from 23 to 37 wt.% MnO, and present high amounts of Ni (12–21 wt.% NiO) and Co (1–8 wt.% CoO). In the analysed samples, Al and Fe contents ranged from 4 to 17 wt.% $Al_2O_3$ and from 3 to 11.4 wt.% $Fe_2O_3$, again inversely correlated.

The chemical footprint of Mn minerals reported in this study was also similar to other lithiophorite, asbolane–lithiophorite intermediates, and cryptomelane recorded in other localities (Table 4). Most data reported in the literature come from studies from New Caledonia, where Co-bearing minerals occur as colloform or fibrous cryptocrystalline to microcrystalline aggregates, intimately intergrown with Mn–Fe-oxides and other poorly crystallised minerals, which appear as spots or coatings, onion peel structures, pseudomorphs of silicates or (rhizo)concretions [51]. The identified Co-bearing minerals in New Caledonia were phyllomanganates (asbolane, lithiophorite and intermediates) with a variable range of compositions between Ni and Co; being lithiophorite, more abundant in those weathering profiles with plagioclase lherzolite as a protolith ([51] and references therein), although other Co and Mn minerals were also identified (heterogenite, cryptomelane, ramsdellite, todorokite). Several authors [38,51–55] have investigated the crystal chemistry and composition of several samples of Ni and Co-bearing minerals of Poro, Tiébaghi and Koniambo.

In the Nkamouna deposit (Cameroon), lithiophorite is the main Mn-phase, and is commonly endowed in Co. It was identified as bluish to black cryptocrystalline to fine-grained concretions, commonly associated with gibbsite and magnetite [56]. Other phases were pyrolusite, cryptomelane (associated with pyrolusite) and lithiophorite–asbolane intermediates.

In the Wingellina oxide-type laterite deposits (Western Australia), Mn-oxyhydroxides were studied by [15], who identified lithiophorite–asbolane intermediate dominant phases and some other minor phases such as romanèchite, ernienickelite–jianshuiite, manganite, and birnessite. Mn-oxyhydroxides of the Palawan deposit (Philippines) were studied by [57], who identified lithiophorite–asbolane intermediates as the main host of Ni and Co in the oxide horizon, while [58,59] studied the asbolane from the products of weathering

of the Lipovsk serpentine deposit (Middle Urals, Russia), which occur as platy fragments associated with goethite.

**Table 4.** Manganese, Co and Ni contents of Mn-bearing minerals from different laterite deposits (number of samples within parentheses).

| Mn-Bearing Minerals | Laterite Deposit | $MnO_2$ (wt.%) | CoO (wt.%) | NiO (wt.%) | Reference |
|---|---|---|---|---|---|
| Asbolane | Lipovsk (Middle Urals, Russia) (1) | 94.2 | – | 6.3 | [59] |
| | Lipovsk (Middle Urals, Russia) (2) | 46.9–49.1 | 6.9 | 11.4 | [58] |
| | Urals (Russia) (3) | 55.1–66.7 | <6.9 | 11.4–21.6 | [38] |
| | New Caledonia (1) | 48.3 | 21.1 | 10.7 | [53] |
| | New Caledonia (2) | 48.3–66.7 | <21.1 | 10.7–17.9 | [38] |
| | New Caledonia (2) | 58.9–65.2 | 1.2–1.7 | 10.1–12.6 | [54] |
| | New Caledonia (3) | 40.1–66.7 | 0.9–5.1 | 17.9–20.1 | [52] |
| | Moa Bay (Cuba) (3) | 31.3–43.3 | 1.2–7.8 | 19.3–20.5 | [47] |
| Birnessite | New Caledonia (3) | 85.1–91.9 | 0.8–1.5 | 0.1–1.0 | [54] |
| Cryptomelane | Nkamouna (Cameroon) (5) | 34.0–80.9 | 2.7–16.9 | 1.1–6.9 | [56] |
| Heterogenite | New Caledonia (1) | 0.2 | 69.3 | 4.7 | [38,52,53] |
| | Shaba (Democratic Republic of the Congo) (1) | 0.5 | 76.4 | 1.9 | [38] |
| Lithiophorite | New Caledonia (1) | 46.0 | 7.1 | 1.5 | [38,52] |
| | Postmasburg (South Africa) (1) | 47.0 | – | – | [38] |
| | Nkamouna (Cameroon) (12) | 29.3–50.5 | 3.1–10.8 | 1.7–7.9 | [56] |
| | New Caledonia (2) | 44.1–46.0 | 7.1–8.9 | 1.3–1.4 | [53] |
| | Loma Ortega (Dominican Republic) (27) | 14.1–85.6 | 0.1–6.5 | 0.6–23.2 | [46] |
| Lithiophorite–asbolane intermediate | Palawan (Philippines) (4) | 34.3–44.7 | 1.3–8.1 | 3.7–19.5 | [57] |
| | New Caledonia (1) | 45.4 | 12.6 | 2.7 | [52] |
| | Wingellina (Australia) (8) | 33.7–55.1 | 0.1–2.5 | 10.5–14.1 | [15] |
| | Nkamouna (Cameroon) (5) | 20.2–43.8 | 2.3–17.0 | 0.7–7.5 | [56] |
| Romanechite | Wingellina (Australia) (4) | 51.9–69.3 | 0.7–1.6 | 1.1–2.9 | [15] |
| Phyllomanganate | New Caledonia (4) | 74.6–88.7 | 1.2–1.5 | 1.4–6.2 | [53] |
| Pyrolusite | Nkamouna (Cameroon) (2) | 70.0–96.4 | 0.7–1.2 | 0.9–1.0 | [56] |
| Ramsdellite | New Caledonia (1) | 95.3 | 0.8 | – | [52] |
| Todorokite | New Caledonia (1) | 61.9 | 0.9 | 0.4 | [52] |
| Co–Ni-bearing Mn-hydroxides | Wingellina (Australia) (6) | 54.1–90.8 | 0.2–3.0 | 2.3–14.1 | [15] |
| Mn-oxide | New Caledonia (1) | 38.7 | 11.9 | 5.8 | [53] |
| Unspecified | New Caledonia (9) | 13.6–38.8 | 4.2–10.1 | 15.9–22.6 | [55] |

### *5.3. Formation of Co-Mn Bearing Minerals in Laterite Deposits*

Mn-bearing minerals in Loma Caribe and Loma de Hierro were mainly found in the transition from the oxide horizon to the saprolite (Figure 2). Their formation at this level within the laterite profile is not uncommon, as it has also been observed in other deposits worldwide [55,60].

The shift of soil solution from acidic to slightly alkaline is the main trigger for the formation of Mn oxides at this interface in the laterite profile ([55] and references therein). In the oxide zone, Mn is commonly sunk by goethite, hematite or other Fe-oxyhydroxides. Due to weathering, temperature, and humidity, Mn can be leached from Fe-bearing minerals and transported downwards as colloidal complexes or aqueous complexes [55,61,62]. In the transition to the saprolite horizon, due to the increase in pH and solution saturation, Mn-oxides precipitation may occur [61]. Although being thermodynamically favoured, oxidation of Mn(II) is very slow in natural waters, but Fe(III) and especially bacterial and fungal activity can accelerate this process by several orders of magnitude [61,63,64]. The presence of lithiophorite, however, suggests that the oxidation of Mn(II) is a slow process [58], as the structure of this mineral needs time to form.

Figure 14 shows predominance diagrams (Eh–pH) of the Mn–Co–$H_2O$ system calculated with the Gibbs Studio code [30] based on Phreeqc [31] and the llnl.dat database

from [31]. The thermodynamic data for Co aqueous species $Co(OH)_3^-$ and $Co(OH)^+$ were taken from the ThermoChimie database [65] and [66]. Due to the lack of thermodynamic data for lithiophorite, asbolane or lithiophorite–asbolane intermediate compounds, birnessite was considered instead, in the construction of predominance diagram. Birnessite, being part of the same phyllomanganate group, can be thus considered representative also for lithiophorite and lithiophorite–asbolane [48]. Furthermore, it has to be emphasised that lithiophorite is considered to form after the alteration of birnessite (and other less mature Mn phases as romanechite) [55]. Calculations were performed allowing only the formation of birnessite, $Mn(OH)_3$(s) and $Mn(OH)_2$(s). Other Mn solid phases such as pyrolusite, todorokite, hausmannite and manganite were not allowed to precipitate since their higher thermodynamic stability inhibits the formation of birnessite. The outcome of the thermodynamic calculation showed that an increase in pH in the oxidised zone allows the formation of Mn-oxyhydroxides.

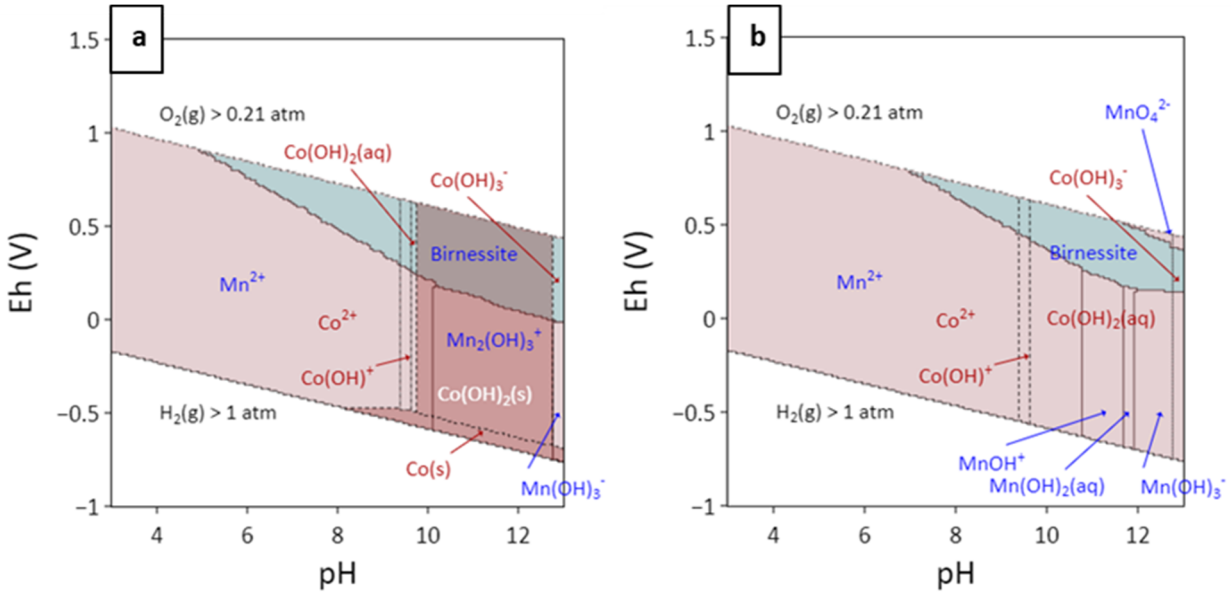


**Figure 14.** Predominance diagram (Eh–pH) of the Mn–Co–$H_2O$ system calculated with Gibbs Studio [30] and the llnl.dat database from [31] with some modifications (see text for explanation), at 25 °C, with a total aqueous concentration of Mn and Co of $10^{-6}$ M (**a**) and $10^{-10}$ M (**b**).

The type of mineral that precipitates depends on the chemical conditions, water composition, Eh and pH. The authors of [56] also observed rim/core textures in the Nkamouna laterite (Cameroon), with pyrolusite at the centre of cryptomelane-lined cavities. The authors considered that as the presence of other cations inhibits the formation of pure Mn-solid phases, pyrolusite should have formed after the precipitation of cryptomelane, which would have removed other cations from the solution. In Loma Caribe and Loma de Hierro, core grains were richer in Mn than rims. This observation agrees with those of [15,56]. However, textural features suggest that rims overgrew the core instead of being formed first (Figure 9c).

In Loma Caribe and Loma de Hierro, lithiophorite and lithiophorite–asbolane intermediates were the most common minerals observed. Most researchers consider that these minerals are a weathering product of previous Mn-oxide minerals [15,56,67,68], but in other cases there is no direct evidence of a primary mineral [57]. In Loma Caribe and Loma de Hierro, Mn-bearing mineral textures did not indicate alteration from previous bearing minerals, so lithiophorite precipitation from soil solution cannot be discarded [56].

Due to its higher content in Al, it is considered that the stability of lithiophorite is higher than that of other Mn minerals, as Al inhibits electron transfer hindering Mn(III) reduction, and, therefore, mineral dissolution under supergene regime ([52] and references therein).

Formation of lithiophorite implies the incorporation of Al in the system. In either Loma Caribe or Loma de Hierro, Al-bearing minerals such as gibbsite and Mn-bearing phyllosilicates have been identified, confirming the availability of Al in the system, that ultimately may come from clinopyroxene and plagioclase minerals from the protolith (lherzolite, clinopyroxene-rich harzburgite, gabbro and diorite) [23–25,69,70].

Mn-oxyhydroxides, and in particular those of biogenic origin, present a high sorption capacity because of their structure, variable (but low) crystallinity with a large surface area, and a very low point of zero charge that promotes negative charged surface areas under common soil pH values [64,71,72]. Phyllomanganates also present a high cation exchange capacity [73]. Cobalt is easily adsorbed onto Mn-bearing minerals' surfaces, and despite Co(II) being the most thermodynamically stable oxidation state in environmental conditions, it is easily oxidised to Co(III) by reduction of Mn(IV) to Mn(III) under supergene conditions [7,71]. With ageing, Co enrichment increases, and the initially adsorbed Co becomes permanently bound [56,74]. Repetition of this process would have led to an enrichment of Co in relation to Mn. This is consistent with the highest content of Co in the saprolite samples from Loma Caribe (Figure 11b). At higher pH, precipitation of Co hydroxide minerals is enhanced (Figure 14a), which might represent an explanation of the Co enrichment in saprolite [51]. Cobalt behaviour is also affected by Eh conditions. Under reducing conditions, Co is released into solution because Co(III) is directly reduced or by reductive dissolution of Mn and/Fe oxides (Figure 14) [75]. All these oxidation–reduction processes take place under supergene conditions, implying good drainage and oxygenated conditions, such as those near a fluctuating water table [51,56]. Therefore, Co–Mn-bearing minerals can be considered a reliable indicator of the position of the paleo-water table within a laterite profile.

Similar to Ni, the primary sources of Mn and Co in Loma Caribe and Loma de Hierro can be found in the protolith [16,17]. Continuous weathering under tropical conditions leaches most of the soluble elements of the protolith, and the least soluble ones, such as Fe and Al, accumulate, forming their own minerals [6,51]. Nickel, Mn and Co are first retained (e.g., sorption processes and/or replacement of Fe) in Fe and Al-bearing minerals [6], and ultimately leached and concentrated in the saprolite-to-oxide zone interface.

## 6. Conclusions

The Co mineralisations in the Ni–Co laterite profiles of Loma Caribe and Loma de Hierro were mainly associated with Mn-oxyhydroxide minerals, with a composition between Ni asbolane and lithiophorite, found in the transition between the saprolite and the oxide zone. In Loma Caribe, Co-bearing Mn-oxyhydroxide minerals showed colloform aggregate, and globular to spherulitic granular textures, while in Loma de Hierro, they displayed banded colloform, fibrous or tabular textures. In Loma de Hierro, Mn–Co phyllosilicates were also identified. Most of the compositional analyses of Mn-oxyhydroxides yielded 20 and 40 wt.% Mn, with Ni and Co up to 16 and 10 wt.%, respectively, and only in a few cases were Mn contents of up to 54 wt.% MnO on average, measured.

These type of Co mineralisations have also been identified in other laterite deposits worldwide. Formation of Mn-oxyhydroxides in the transition zone is mainly due to the change of pH and Eh occurring in this area and to the saturation of pore solution that may lead to the formation of these minerals by precipitation. Co is considered to be firstly sorbed onto Mn-bearing minerals, after being oxidised because of Mn reduction under supergene conditions, becoming permanently bound into Mn-minerals. Therefore, these minerals are considered to be an indicator of the water level during laterite profile formation.

**Author Contributions:** Conceptualisation, C.D., C.V.-d.-B. and J.A.P.; methodology, C.D., C.V.-d.-B., E.T. and L.L.; software, C.D.; investigation, C.D., C.V.-d.-B., L.L., S.G., J.M.S., J.I.-I. and M.C., resources, J.A.P.; writing—original draft preparation and editing, C.D., C.V.-d.-B. and J.A.P.; writing—review, E.T., J.M.S., S.G., J.I.-I. and M.C.; supervision, J.A.P.; project administration, J.A.P.; funding acquisition, J.A.P. All authors have read and agreed to the published version of the manuscript.

**Funding:** This research was supported by grant PID2019-105625RB-C21 funded by MCIN/AEI/10.13039/501100011033 and by the Caribbean Lithosphere Reserve Group (http://caribbeanlithos.com/). IDAEA-CSIC is a Severo Ochoa Center of Research Excellence (Spanish Ministry of Science and Innovation, Project CEX2018-000794-S).

**Data Availability Statement:** Not applicable.

**Acknowledgments:** We are grateful to Maite Garcia Vallès and to the staff of the Centres Científics i Tecnològics of the Universitat de Barcelona, Barcelona (Spain) (CCiT-UB) for their assistance in measurements. Micro-XRD measurements were performed at BL04-MPSD beamline of ALBA Synchrotron, Cerdanyola del Vallès, Barcelona (experiment AV-2019023550). We would like to thank Oriol Vallcorba and Catalin Popescu for their support during the XRD experiments at ALBA Synchrotron. IDAEA-CSIC is a Severo Ochoa Center of Research Excellence (Spanish Ministry of Science and Innovation, Project CEX2018-000794-S). We are also grateful to the reviewers for improving the quality of this manuscript.

**Conflicts of Interest:** The authors declare no conflict of interest.

## References

1. European Commission. Report from the Commission to the European Parliament, the Council, the European Economic and Social Committee and the Committee of the Regions: Critical Raw Materials Resilience: Charting a Path towards greater Security and Sustainability. Available online: https://eur-lex.europa.eu/legal-content/EN/TXT/?uri=CELEX:52020DC0474 (accessed on 15 September 2021).
2. Slack, J.F.; Kimball, B.E.; Shedd, K.B. Cobalt. In *Critical Mineral Resources of the United States—Economic and Environmental Geology and Prospects for Future Supply*; Schulz, K.J., DeYoung, J.H., Jr., Seal, R.R., II, Bradley, D.C., Eds.; U.S. Geological Survey Professional Paper: Reston, VA, USA, 2017; Chapter F; pp. F1–F40. [CrossRef]
3. US Geological Survey. *Mineral Commodity Summaries 2020: US Geological Survey*; US Geological Survey: Reston, VA, USA, 2020; 200p. [CrossRef]
4. Alves Dias, P.; Blagoeva, D.; Pavel, C.; Arvanitidis, N. *Cobalt: Demand-Supply Balances in the Transition to Electric Mobility*; EUR 29381 EN; Publications Office of the European Union: Luxembourg, 2018; ISBN 978-92-79-94311-9. [CrossRef]
5. Seck, G.S.; Hache, E.; Barnet, C. Potential bottleneck in the energy transition: The case of cobalt in an accelerating electro-mobility world. *Resour. Policy* **2021**, *75*, 102516. [CrossRef]
6. Santoro, L.; Putzolu, F.; Mondillo, N.; Herrington, R.; Najorka, J.; Boni, M.; Dosbaba, M.; Maczurad, M.; Balassone, G. Quan-titative mineralogical evaluation of Ni-Co laterite ores through XRPD-QPA- and automated SEM-based approaches: The Wingellina (Western Australia) case study. *J. Geochem. Explor.* **2021**, *223*, 106695. [CrossRef]
7. Newsome, L.; Arguedas, A.F.S.; Coker, V.; Boothman, C.; Lloyd, J. Manganese and cobalt redox cycling in laterites; Biogeochemical and bioprocessing implications. *Chem. Geol.* **2019**, *531*, 119330. [CrossRef]
8. Butt, C.R.M.; Cluzel, D. Nickel Laterite Ore Deposits: Weathered Serpentinites. *Elements* **2013**, *9*, 123–128. [CrossRef]
9. Freyssinet, P.; Butt, C.R.M.; Morris, R.C.; Piantone, P. Ore-Forming Processes Related to Lateritic Weathering. In *One Hundredth Anniversary Volume*; Society of Economic Geologists: Littleton, CO, USA, 2005; pp. 681–722. [CrossRef]
10. Golightly, J.P. *Nickeliferous Laterite Deposits*; Society of Economic Geologists: Littleton, CO, USA, 1981; pp. 710–735. [CrossRef]
11. Golightly, J.P.; Goldfarb, R.J.; Marsh, E.E.; Monecke, T. Progress in Understanding the Evolution of Nickel Laterites. In *The Challenge of Finding New Mineral Resources: Global Metallogeny, Innovative Exploration, and New Discoveries*; Society of Economic Geologists: Littleton, CO, USA, 2010; Volume 15, pp. 451–485. [CrossRef]
12. Villanova-De-Benavent, C.; Domènech, C.; Tauler, E.; Galí, S.; Tassara, S.; Proenza, J.A. Fe–Ni-bearing serpentines from the saprolite horizon of Caribbean Ni-laterite deposits: New insights from thermodynamic calculations. *Miner. Depos.* **2016**, *52*, 979–992. [CrossRef]
13. Dehaine, Q.; Tijsseling, L.T.; Glass, H.J.; Törmänen, T.; Butcher, A.R. Geometallurgy of cobalt ores: A review. *Miner. Eng.* **2020**, *160*, 106656. [CrossRef]
14. Elias, M.; Donaldson, M.J.; Giorgetta, N.E. Geology, mineralogy, and chemistry of lateritic nickel-cobalt deposits near Kalgoorie, Western Australia. *Econ. Geol.* **1981**, *76*, 1775–1783. [CrossRef]
15. Putzolu, F.; Balassone, G.; Boni, M.; Maczurad, M.; Mondillo, N.; Najorka, J.; Pirajno, F. Mineralogical association and Ni-Co deportment in the Wingellina oxide-type laterite deposit (Western Australia). *Ore Geol. Rev.* **2018**, *97*, 21–34. [CrossRef]
16. Aiglsperger, T.; Proenza, J.A.; Lewis, J.F.; Labrador, M.; Svojtka, M.; Rojas-Purón, A.; Longo, F.; Ďurišová, J. Critical metals (REE, Sc, PGE) in Ni laterites from Cuba and the Dominican Republic. *Ore Geol. Rev.* **2016**, *73*, 127–147. [CrossRef]
17. Domènech, C.; Galí, S.; Soler, J.M.; Ancco, M.P.A.; Meléndez, W.; Rondón, J.; Villanova-De-Benavent, C.; Proenza, J.A. The Loma de Hierro Ni-laterite deposit (Venezuela): Mineralogical and chemical composition. *Boletín Soc. Geológica Mex.* **2020**, *72*, A050620. [CrossRef]

18. Villanova-de-Benavent, C.; Proenza, J.A.; Galí, S.; García-Casco, A.; Tauler, E.; Lewis, J.F.; Longo, F. Garnierites and garnierites: Textures, mineralogy and geochemistry of garnierites in the Falcondo Ni laterite deposit, Dominican Republic. *Ore Geol. Rev.* **2014**, *58*, 91–109. [CrossRef]
19. Lewis, J.F.; Jiménez, J.G. Duarte complex in the La Vega–Jarabacoa–Janico Area, Central Hispaniola: Geological and geochemical features of the sea floor during the early stages of arc evolution. In *Geologic and Tectonic Development of the North America–Caribbean Plate Boundary in Hispaniola*; Mann, P., Draper, G., Lewis, J.F., Eds.; Geological Society of America Special Papers: Boulder, CO, USA, 1991; Volume 262, pp. 115–142.
20. Hackley, P.C.; Urbani, F.; Karlsen, A.W.; Garrity, C.P. *Mapa Geologico de Venezuela a Escala 1:750,000*; USGS Publications Open-File Report 2006-1109 Warehouse: Virgina, VA, USA, 2006. [CrossRef]
21. Giunta, G.; Beccaluva, L.; Coltorti, M.; Mortellaro, D.; Siena, F.; Cutrupia, D. The peri-Caribbean ophiolites: Structure, tectono-magmatic significance and geodynamic implications. *Caribb. J. Earth Sci.* **2000**, *36*, 1–20.
22. Urbani, F. Una revisión de los terrenos geológicos del sistema montañoso del Caribe, Norte de Venezuela. *Boletín Geología* **2018**, *23*, 118–216.
23. Marvin, B.; Valencia, V.; Grande, S.; Urbani, F.; Hurtado, R. Geocronología U–Pb en cristales de zircón de la metadiorita de la Guacamaya, gabro de la ofiolita de Loma de Hierro y gabro de El Chacao, estados Aragua y Guárico. In Proceedings of the V Simposio Venezolano de Geociencias de las Rocas Ígneas y Metamórficas, Caracas, Venezuela, 28–29 November 2013.
24. Neill, I.; Kerr, A.C.; Chamberlain, K.R.; Schmitt, A.K.; Urbani, F.; Hastie, A.R.; Pindell, J.L.; Barry, T.L.; Millar, I.L. Vestiges of the proto-Caribbean seaway: Origin of the San Souci Volcanic Group, Trinidad. *Tectonophysics* **2014**, *626*, 170–185. [CrossRef]
25. Urbani, F.; Rodríguez, J.A. *Atlas Geológico de la Cordillera de la Costa*; Ediciones Fundación Geos y Funvisis: Caracas, Venezuela, 2004; 146p.
26. Cheary, R.W.; Coelho, A.A. A fundamental parameters approach to X-ray line-profile fitting. *J. Appl. Crystallogr.* **1992**, *25*, 109–121. [CrossRef]
27. Coelho, A.A. *TOPAS-Academic, version 4.2*; TOPAS-Academic: Brisbaine, Australia, 2007.
28. Rius, J.; Vallcorba, O.; Frontera, C.; Peral, I.; Crespi, A.; Miravitlles, C. Application of synchrotron through-the-substrate microdiffraction to crystals in polished thin sections. *IUCrJ* **2015**, *2*, 452–463. [CrossRef]
29. Prescher, C.; Prakapenka, V.B. DIOPTAS: A program for reduction of two-dimensional X-ray diffraction data and data ex-ploration. *High Press. Res.* **2015**, *35*, 223–230. [CrossRef]
30. Nardi, A.; de Vries, L.M. *GibbsStudio, version 3.1.1*; Barcelona Science Technologies SL: Barcelona, Spain, 2017. Available online: https://gibbsstudio.io/ (accessed on 31 October 2020).
31. Parkhurst, D.L.; Appelo, C.A.J. Description of input and examples for PHREEQC version 3—A computer program for specia-tion, batch-reaction, one-dimensional transport, and inverse geochemical calculations. *US Geol. Surv. Tech. Methods* **2013**, *6*, 497. Available online: https://pubs.usgs.gov/tm/06/a43/pdf/tm6-A43.pdf (accessed on 1 July 2022).
32. Burlet, C.; Vanbrabant, Y. Study of the spectro-chemical signatures of cobalt-manganese layered oxides (asbolane-lithiophorite and their intermediates) by Raman spectroscopy. *J. Raman Spectrosc.* **2015**, *46*, 941–952. [CrossRef]
33. Katsiapi, A.; Tsakiridis, P.; Oustadakis, P.; Agatzini-Leonardou, S. Cobalt recovery from mixed Co–Mn hydroxide precipitates by ammonia–ammonium carbonate leaching. *Miner. Eng.* **2010**, *23*, 643–651. [CrossRef]
34. Wang, Y.; Xing, S.; Zhang, Y.; Li, Z.; Ma, Y.; Zhang, Z. Mineralogical and thermal characteristics of low-grade Jinlong bauxite sourced from Guangxi Province, China. *J. Therm. Anal.* **2015**, *122*, 917–927. [CrossRef]
35. Gialanella, S.; Girardi, F.; Ischia, G.; Lonardelli, I.; Mattarelli, M.; Montagna, M. On the goethite to hematite phase transformation. *J. Therm. Anal. Calorim.* **2010**, *102*, 867–873. [CrossRef]
36. De Aquino, T.F.; Riella, H.; Bernardin, A.M. Mineralogical and Physical–Chemical Characterization of a Bauxite Ore from Lages, Santa Catarina, Brazil, for Refractory Production. *Miner. Process. Extr. Met. Rev.* **2011**, *32*, 137–149. [CrossRef]
37. Földvári, M. *Handbook of Thermogravimetric System of Minerals and Its Use in Geological Practice*; Occasional Papers of the Geological Institute of Hungary; Geological Institute of Hungary: Budapest, Hungary, 2011; ISBN 978-963-671-288-4.
38. Llorca, S.; Monchoux, P. Supergene cobalt minerals from New Caledonia. *Can. Mineral.* **1991**, *29*, 149–161.
39. Ribeiro, P.P.M.; de Souza, L.C.M.; Neumann, R.; dos Santos, I.D.; Dutra, A.J.B. Nickel and cobalt losses from laterite ore after the sulfation-roasting-leaching processing. *J. Mater. Res. Technol.* **2020**, *9*, 12404–12415. [CrossRef]
40. Palchik, N.A.; Moroz, T.N.; Grigorieva, T.N.; Miroshnichenko, L.V. Manganese minerals from the Miassovo freshwater lake: Composition and structure. *Russ. J. Inorg. Chem.* **2014**, *59*, 511–518. [CrossRef]
41. White, W.N.; Vito, C.; Scheetz, B.E. The mineralogy and trace element chemistry of black manganese oxide deposits from caves. *J. Cave Karst Stud.* **2009**, *271*, 136–143.
42. Ling, F.T.; Post, J.E.; Heaney, P.J.; Kubicki, J.D.; Santelli, C.M. Fourier-transform infrared spectroscopy (FTIR) analysis of triclinic and hexagonal birnessites. *Spectrochim. Acta Part A Mol. Biomol. Spectrosc.* **2017**, *178*, 32–46. [CrossRef]
43. Chukanov, N.V. *Infrared Spectra of Mineral Species: Extended Library*; Springer: Dordrecht, The Netherlands, 2014. [CrossRef]
44. Potter, R.M.; Rossman, G.R. The tetravalent manganese oxides: Identification, hydration, and structural relationships by infrared spectroscopy. *Am. Mineral.* **1979**, *64*, 1199–1218.
45. Carmichael, S.K.; Doctor, D.H.; Wilson, C.G.; Feierstein, J.; McAleer, R. New insight into the origin of manganese oxide ore deposits in the Appalachian Valley and Ridge of northeastern Tennessee and northern Virginia, USA. *GSA Bull.* **2017**, *129*, 1158–1180. [CrossRef]

46. Tauler, E.; Lewis, J.F.; Villanova-De-Benavent, C.; Aiglsperger, T.; Proenza, J.A.; Domènech, C.; Gallardo, T.; Longo, F.; Galí, S. Discovery of Ni-smectite-rich saprolite at Loma Ortega, Falcondo mining district (Dominican Republic): Geochemistry and mineralogy of an unusual case of "hybrid hydrous Mg silicate—Clay silicate" type Ni-laterite. *Miner. Depos.* **2017**, *52*, 1011–1030. [CrossRef]
47. Roqué-Rosell, J.; Mosselmans, F.; Proenza, J.A.; Labrador, M.; Galí, S.; Atkinson, K.D.; Quinn, P.D. Sorption of Ni by "lithiophorite-asbolane" intermediates in Moa Bay lateritic deposits, eastern Cuba. *Chem. Geol.* **2010**, *275*, 9–18. [CrossRef]
48. Post, J.E. Manganese oxide minerals: Crystal structures and economic and environmental significance. *Proc. Natl. Acad. Sci. USA* **1999**, *96*, 3447–3454. [CrossRef]
49. Dublet, G.; Juillot, F.; Brest, J.; Noël, V.; Fritsch, E.; Proux, O.; Olivi, L.; Ploquin, F.; Morin, G. Vertical changes of the Co and Mn speciation along a lateritic regolith developed on peridotites (New Caledonia). *Geochim. Cosmochim. Acta* **2017**, *217*, 1–15. [CrossRef]
50. Putzolu, F.; Abad, I.; Balassone, G.; Boni, M.; Mondillo, N. Ni-bearing smectites in the Wingellina laterite deposit (Western Australia) at nanoscale: TEM-HRTEM evidences of the formation mechanisms. *Appl. Clay Sci.* **2020**, *196*, 105753. [CrossRef]
51. Maurizot, P.; Sevin, B.; Lesimple, S.; Bailly, L.; Iseppi, M.; Robineau, B. Chapter 10 Mineral resources and prospectivity of the ultramafic rocks of New Caledonia. In *New Caledonia: Geology, Geodynamic Evolution and Mineral Resource*; Maurizot, P., Mortimer, N., Eds.; Geological Society: London, UK, 2020; Volume 51, pp. 247–277. [CrossRef]
52. Llorca, S.M. Metallogeny of supergene cobalt mineralization, New Caledonia. *Aust. J. Earth Sci.* **1993**, *40*, 377–385. [CrossRef]
53. Manceau, A.; Llorca, S.; Calas, G. Crystal chemistry of cobalt and nickel in lithiphorite and asbolane from New Caledonia. *Geoch. Cosmoch. Acta* **1987**, *51*, 105–113. [CrossRef]
54. Ploquin, F.; Fritsch, E.; Guigner, J.M.; Esteve, I.; Delbes, L.; Dublet, G.; Juillot, F. Phyllomanganate vein-infillings in faulted and Al-poor regoliths of the New Caledonian ophiolite: Periodic and sequential crystallization of Ni–asbolane, Alk–birnessite and H–birnessite. *Eur. J. Mineral.* **2019**, *31*, 335–352. [CrossRef]
55. Ulrich, M.; Cathelineau, M.; Muñoz, M.; Boiron, M.-C.; Teitler, Y.; Karpoff, A.M. The relative distribution of critical (Sc, REE) and transition metals (Ni, Co, Cr, Mn, V) in some Ni-laterite deposits of New Caledonia. *J. Geochem. Explor.* **2018**, *197*, 93–113. [CrossRef]
56. Dzemua, G.L.; Gleeson, S.A.; Schofield, P.F. Mineralogical characterization of the Nkamouna Co–Mn laterite ore, southeast Cameroon. *Miner. Depos.* **2012**, *48*, 155–171. [CrossRef]
57. Tupaz, C.A.J.; Watanabe, Y.; Sanematsu, K.; Echigo, T. Mineralogy and geochemistry of the Berong Ni-Co laterite deposit, Palawan, Philippines. *Ore Geol. Rev.* **2020**, *125*, 103686. [CrossRef]
58. Chukhrov, F.V.; Gorshkov, A.I.; Vitovskaya, I.V.; Drits, V.A.; Sivtsov, A.V. On the Nature of Co-Ni Asbolane; a Component of Some Supergene Ores. In *Ore Genesis: The State of the Art*; Amstutz, G.C., El Goresy, A., Frenzel, G., Kluth, C., Moh, G., Wauschkuhn, A., Zimmermann, R.A., Eds.; Springer: Berlin/Heidelberg, Germany, 1982; pp. 230–239. [CrossRef]
59. Gorshkov, A.I.; Bogdanov, Y.A.; Sivtsov, A.V.; Mokhov, S.V. A new Mg-AI-Ni asbolane. *Doklady Akad. Nauk* **1995**, *342*, 781–784. (In Russian)
60. Marsh, E.; Anderson, E.; Gray, F. Chapter H of Mineral deposit models for resource assessment. In *Nickel-Cobalt Laterites—A Deposit Model*; 2010–5070–H; Paper for U.S. Geological Survey Scientific Investigations: Denver, CO, USA, 2013; 38p. Available online: https://pubs.usgs.gov/sir/2010/5070/h/ (accessed on 28 June 2022).
61. Burns, R.G.; Burns, V.M. Manganese oxides. In *Marine Minerals*; Ribbe, P.H., Ed.; Mineralogical Society of America: Washington, DC, USA, 1979.
62. Quantin, C.; Becquer, T.; Berthelin, J. Mn-oxide: A major source of easily mobilizable Co and Ni under reducing conditions in New Caledonia Ferralsols. *Comptes Rendus Geosci.* **2002**, *334*, 273–278. [CrossRef]
63. Aoshima, M.; Tani, Y.; Fujita, R.; Tanaka, K.; Miyata, N.; Umezawa, K. Simultaneous Sequestration of $Co^{2+}$ and $Mn^{2+}$ by Fungal Manganese Oxide through Asbolane Formation. *Minerals* **2022**, *12*, 358. [CrossRef]
64. Villalobos, M.; Bargar, J.; Sposito, G. Trace Metal Retention on Biogenic Manganese Oxide Nanoparticles. *Elements* **2005**, *1*, 223–226. [CrossRef]
65. Giffaut, E.; Grivé, M.; Blanc, P.; Vieillard, P.; Colàs, E.; Gailhanou, H.; Gaboreau, S.; Marty, N.; Madé, B.; Duro, L. Andra thermodynamic database for performance assessment: ThermoChimie. *Appl. Geochem.* **2014**, *49*, 225–236. [CrossRef]
66. Plyasunova, N.V.; Zhang, Y.; Muhammed, M. Critical evaluation of thermodynamic of complex formation of metals ions in aqueous solution: IV hydrolysis and hydroxo-complex of $Ni^{2+}$ at 298.15K. *Hydrometallurgy* **1998**, *48*, 153–169. [CrossRef]
67. Cui, H.; You, L.; Feng, X.; Tan, W.; Qiu, G.; Liu, F. Factors Governing the Formation of Lithiophorite at Atmospheric Pressure. *Clays Clay Miner.* **2009**, *57*, 353–360. [CrossRef]
68. Rao, D.; Nayak, B.; Acharya, B. Cobalt-rich lithiophorite from the Precambrian Eastern Ghats manganese ore deposit of Nishikhal, south Orissa, India. *Mineralogia* **2010**, *41*, 11–21. [CrossRef]
69. Farré-De-Pablo, J.; Proenza, J.A.; González-Jiménez, J.M.; Aiglsperger, T.; Garcia-Casco, A.; Escuder-Viruete, J.; Colás, V.; Longo, F. Ophiolite hosted chromitite formed by supra-subduction zone peridotite–plume interaction. *Geosci. Front.* **2020**, *11*, 2083–2102. [CrossRef]
70. Marchesi, C.; Garrido, C.J.; Proenza, J.A.; Hidas, K.; Varas-Reus, M.I.; Butjosa, L.; Lewis, J.F. Geochemical record of subduction initiation in the sub-arc mantle: Insights from the Loma Caribe peridotite (Dominican Republic). *Lithos* **2016**, *252-253*, 1–15. [CrossRef]

71. Decrée, S.; Pourret, O.; Baele, J.-M. Rare earth element fractionation in heterogenite (CoOOH): Implication for cobalt oxidized ore in the Katanga Copperbelt (Democratic Republic of Congo). *J. Geochem. Explor.* **2015**, *159*, 290–301. [CrossRef]
72. Nicholson, K. Contrasting mineralogical-geochemical signatures of manganese oxides; guides to metallogenesis. *Econ. Geol.* **1992**, *87*, 1253–1264. [CrossRef]
73. Tebo, B.M.; Bargar, J.R.; Clement, B.G.; Dick, G.J.; Murray, K.J.; Parker, D.; Verity, R.; Webb, S.M. Biogenic Manganese Oxides: Properties and Mechanisms of Formation. *Annu. Rev. Earth Planet. Sci.* **2004**, *32*, 287–328. [CrossRef]
74. Wu, Z.; Lanson, B.; Feng, X.; Yin, H.; Tan, W.; He, F.; Liu, F. Transformation of the phyllomanganate vernadite to tectomanganates with small tunnel sizes: Favorable geochemical conditions and fate of associated Co. *Geochim. Cosmochim. Acta* **2021**, *295*, 224–236. [CrossRef]
75. Beak, D.G.; Kirby, J.K.; Hettiarachchi, G.M.; Wendling, L.; McLaughlin, M.J.; Khatiwada, R. Cobalt Distribution and Speciation: Effect of Aging, Intermittent Submergence, In Situ Rice Roots. *J. Environ. Qual.* **2011**, *40*, 679–695. [CrossRef]